1 **Suppression of transcytosis regulates zebrafish blood-brain barrier development**
2

3

4

5

6

7 Natasha M. O'Brown[1], Sean G. Megason[2*], Chenghua Gu[1*]

8 [1] Department of Neurobiology, [2] Department of Systems Biology, Harvard Medical School, 220
9 Longwood Ave, Boston, MA 02115, U.S.A.
10
11 * denotes corresponding author
12
13 Correspondence:
14
15 Chenghua Gu (chenghua_gu@hms.harvard.edu)

16 Department of Neurobiology, Harvard Medical School

17 Boston, MA 02115, U.S.A.

18 (Phone) 617-432-6364 (Fax) 617-432-1639

19

20 Sean Megason (sean_megason@hms.harvard.edu)

21 Department of Systems Biology, Harvard Medical School

22 Boston, MA 02115, U.S.A.

23 (Phone) 617-432-7441

24   **Abstract:**

25   As an optically transparent model organism with an endothelial blood-brain barrier (BBB),

26   zebrafish offer a powerful tool to study the vertebrate BBB. However, the precise developmental

27   profile of functional zebrafish BBB acquisition and the subcellular and molecular mechanisms

28   governing the zebrafish BBB remain poorly characterized. Here we find a spatiotemporal gradient

29   of barrier acquisition. Moreover, we capture the dynamics of developmental BBB leakage using

30   live imaging, revealing a combination of steady accumulation in the parenchyma and sporadic

31   bursts of tracer leakage. Electron microscopy studies further reveal that this steady accumulation

32   results from high levels of transcytosis that are eventually suppressed, sealing the BBB. Finally,

33   we demonstrate a key mammalian BBB regulator Mfsd2a, which inhibits transcytosis, plays a

34   conserved role in zebrafish. *Mfsd2aa* mutants display increased larval and adult BBB permeability

35   due to increased transcytosis. Our findings indicate a conserved developmental program of

36   barrier acquisition between zebrafish and mice.

Introduction

Blood vessels in the vertebrate brain are composed of a single layer of endothelial cells that possess distinct functional properties that allow the passage of necessary nutrients yet prevent unwanted entry of specific toxins and pathogens into the brain. This specialized endothelial layer forms the blood-brain barrier (BBB) and restricts the passage of substances between the blood and the brain parenchyma via two primary mechanisms: 1) specialized tight junction complexes between apposed endothelial cells to prevent intercellular transit (Reese and Karnovsky, 1967; Brightman and Reese, 1969) and 2) suppressing vesicular trafficking or transcytosis to prevent transcellular transit (Ben-Zvi et al., 2014; Andreone et al., 2015; Andreone et al., 2017). BBB selectivity is further refined with expression of substrate-specific transporters that dynamically regulate the influx of necessary nutrients and efflux of metabolic waste products (Sanchez-Covarrubias et al., 2014; Umans et al., 2017). While the BBB is comprised of endothelial cells, the surrounding perivascular cells including pericytes and astroglial cells, play a critical role in forming and maintaining barrier properties (Janzer and Raff, 1987; Armulik et al., 2010; Bell et al., 2010; Daneman et al., 2010; Wang et al., 2014). Collectively, endothelial cells and the surrounding perivascular cells form the neurovascular unit.

As the simplest genetic model organism with an endothelial BBB (Jeong et al., 2008), zebrafish offer a powerful tool to study the cellular and molecular properties of the vertebrate BBB (Xie et al., 2010; Vanhollebeke et al., 2015; Umans et al., 2017; O'Brown et al., 2018; Quiñonez-Silvero et al., 2019). Zebrafish have served as a great model system to study vascular biology due to their large clutch size, rapid and external development, and transparency for *in vivo* whole organism live-imaging (Lawson and Weinstein, 2002; Jin et al., 2005; Santoro et al., 2007; Armer et al., 2009; Herbert et al., 2009; Phng et al., 2009; Geudens et al., 2010; Herbert et al., 2012; Wilkinson and van Eeden, 2014; Franco et al., 2015; Vanhollebeke et al., 2015; Matsuoka et al., 2016; Ulrich et al., 2016; Galanternik et al., 2017; Stratman et al., 2017; Geudens et al., 2018).

3

63   Additionally, with the advent of CRISPR-Cas9 technology, zebrafish provide an efficient genetic

64   toolkit for targeted mutagenesis (Hwang et al., 2013; Gagnon et al., 2014; Ablain et al., 2015;

65   Varshney et al., 2015; Albadri et al., 2017; Hogan and Schulte-Merker, 2017). However, the

66   subcellular and molecular mechanisms governing the formation and maintenance of the zebrafish

67   BBB remain poorly characterized. Expanding our understanding of the zebrafish BBB can thus

68   reveal the mechanistic similarities between the zebrafish and mammalian BBB to further elevate

69   the position of zebrafish as a model organism for studying the BBB.

70

71   Barrier properties of brain endothelial cells are induced by extrinsic signals from other cells in the

72   surrounding microenvironment during development (Stewart and Wiley, 1981). In rodents, the

73   BBB becomes functionally sealed in a spatiotemporal gradient, with the hindbrain and midbrain

74   barriers becoming functional before the cortical barrier (Daneman et al., 2010; Ben-Zvi et al.,

75   2014; Sohet et al., 2015). Within the cortex, barrier function is acquired along a ventral-lateral to

76   dorsal-medial gradient (Ben-Zvi et al., 2014). In the zebrafish, existing studies have disagreed

77   over the timing of zebrafish barrier formation, with some suggesting that BBB maturation occurs

78   at 3 days post fertilization (dpf) (Jeong et al., 2008; Umans et al., 2017) and others providing a

79   wide range beginning at 3 dpf and extending to 10 dpf (Fleming et al., 2013). These conflicting

80   reports may be due to regional developmental gradients of barrier acquisition or differences in the

81   experimental approaches used to assess BBB permeability such as the molecular weight of

82   tracers and circulation time. To date, a thorough regional characterization of functional barrier

83   acquisition has been lacking in zebrafish.

84

85   Recent work in the mammalian blood-retinal barrier has indicated that suppression of transcytosis

86   governs functional barrier development (Chow and Gu, 2017). Interestingly endothelial cells at

87   the leaky neonatal angiogenic front possess functional tight junction complexes halting the

88   intercellular passage of the tracer protein Horseradish Peroxidase (HRP) at the so-called "kissing

4

89   points". In contrast, these endothelial cells exhibit high levels of HRP-filled vesicles compared to

90   functionally sealed proximal vessels. Moreover, these areas of elevated vesicular trafficking

91   continue to correspond with barrier permeability at the angiogenic front until the barrier seals

92   (Chow and Gu, 2017). Work in the mouse BBB has also demonstrated the importance of

93   suppressing transcytosis in determining barrier permeability. Mice lacking the major facilitator

94   super family domain containing 2a (Mfsd2a) lipid transporter exhibit increased levels of caveolae

95   vesicles in CNS endothelial cells, resulting in increased barrier permeability (Ben-Zvi et al., 2014;

96   Andreone et al., 2017). The subcellular and molecular mechanisms of zebrafish BBB acquisition

97   have yet to be elucidated.

98

99   Here in zebrafish, we find a spatiotemporal gradient of barrier acquisition, and capture the

100   dynamics of developmental BBB leakage using time lapse live imaging. We further find a

101   conserved role for transcytosis suppression in determining barrier properties, both during normal

102   development and in *mfsd2aa* mutants.

103

104   **Results**

105   *Posterior-Anterior Gradient of Zebrafish BBB Development*

106   To determine when and how the zebrafish BBB becomes functional in different brain regions, we

107   performed intracardiac injections of fluorescently-conjugated tracers (1 kDa NHS and 10 kDa

108   Dextran) simultaneously at different developmental stages and imaged live fish after one hour of

109   tracer circulation (Figure 1A and 1B). We used a combination of different molecular weight tracers

110   to tease apart potential avenues of leakage, as tight junctional defects result specifically in the

111   leakage of low molecular weight tracers 1 kDa and below into the brain parenchyma (Nitta et al.,

112   2003; Campbell et al. 2008; Sohet et al., 2015; Yanagida et al. 2017). At 3 dpf, we observed a

113   sealed barrier in the hindbrain as previously described (Jeong et al., 2008), with only a few of the

114   parenchymal cells taking up the injected tracer (average of 2 ± 0.3 cells/embryo with NHS and 2

5

115   ± 0.4 cells/embryo with Dextran; Figure 1 – Supplement 1), which we quantify as a proxy of tracer

116   leakage into the brain. However, in the midbrain we observed an increased number of

117   parenchymal cells that accumulated the circulating tracers (average of 24 ± 1 cells/embryo with

118   NHS and 24 ± 1 cells/embryo with Dextran; Figure 1C and 1D), indicating that the tracers leaked

119   out of the blood vessels into the brain and that the midbrain barrier is not yet functional. In addition

120   to the use of exogenous injected fluorescent tracers, we also assayed BBB permeability with an

121   endogenous transgenic serum DBP-EGFP fusion protein (Tg(*l-fabp:DBP-EGFP*)) to account for

122   injection artifacts (Xie et al., 2010). At 3 dpf, we observed similar leakage patterns with the

123   transgenic serum protein as we did with the injected tracers (average of 24 ± 1 cells/embryo in

124   the midbrain and average of 2 ± 0.4 cells/embryo in the hindbrain; Figure 1C and D; Figure 1 –

125   Supplement 1). At 4 dpf, the BBB in the hindbrain is completely functional with few tracer-filled

126   parenchymal cells (average of 3 ± 0.4 cells/embryo with NHS, 2 ± 0.4 cells/embryo with Dextran

127   and DBP-EGFP; Figure 1 – Supplement 1). However, the midbrain BBB remains leaky (average

128   of 23 ± 1 cells/embryo with NHS and DBP-EGFP and 24 ± 1 cells/embryo with Dextran; p=0.68

129   compared to 3 dpf, one-way ANOVA; Figure 1C and 1D). However, at 5 dpf the number of

130   midbrain parenchymal cells that uptake the tracers is dramatically reduced (average of 9 ± 1

131   cells/embryo with NHS, Dextran, and DBP-EGFP; p<0.0001, one-way ANOVA; Figure 1B and

132   1C) and no change was observed in the hindbrain (Figure 1 – Supplement 1). No significant

133   change was observed in midbrain permeability from 5 to 6 dpf (average of 8 ± 1 cells/embryo with

134   NHS, Dextran, and DBP-EGFP; p=0.904, one-way ANOVA; Figure 1C and 1D), indicating that

135   the midbrain barrier becomes sealed at 5 dpf. We did not assay the forebrain at any of these

136   stages due to the fact that it remains avascularized until 5 dpf. Of note, all three tracers showed

137   nearly indistinguishable patterns of uptake, with similar numbers of cells and many of the same

138   cells simultaneously taking up both injected tracers (Figure 1; Figure 1 – Supplement), suggesting

139   that the leakage is not due to tight junctional defects but may rather be due to an increase in

140   vesicular trafficking.

141   *Time lapse Imaging Reveals Two Modes of Developmental Leakage*

142   The vast majority of studies interrogating BBB permeability have relied on observing leakage in

143   fixed static images from mutant mice, which does not reveal the dynamic nature of the BBB. A

144   huge advantage of zebrafish is the ability to examine biological processes *in vivo* in real-time,

145   providing us with the unique opportunity to observe the process of BBB maturation (Figure 1). To

146   examine the developmental dynamics of barrier leakage, we injected embryos at 3 dpf with

147   fluorescently-labeled 10 kDa Dextran and performed time lapse live imaging for an hour following

148   injection, with time 0 being an average of 8 minutes post-injection. We observed a gradual and

149   diffuse increase in extravascular Dextran intensity over time within the brain parenchyma (slope

150   of 1.301e-4 intensity/sec; Videos 1 and 2; Figure 2A, 2C and 2E). In addition to the time-

151   dependent increase in overall Dextran intensity in the brain parenchyma, we also observed

152   parenchymal cells taking up tracer, both directly adjacent to blood vessels and at a small distance

153   away (Figure 2A and 2C), as in the static images of tracer leakage during development (Figure

154   1). Interestingly, at 3 dpf we observed an actively sprouting cell that extended away from the

155   established vessel in a sporadic fashion (Video 2; Figure 2A). After twenty minutes of rambling

156   migration, this sprout suddenly released a large bolus of Dextran that appeared to be taken up by

157   a single parenchymal cell. Two minutes later, this same sprout released a second bolus of Dextran

158   on the opposite side (Video 2). These rare large bursts of leakage were not unique to this sprout;

159   they were also sporadically observed from established blood vessels (Video 1; Figure 2A). This

160   data revealed two types of leakage occurring during this early developmental stage: steady and

161   diffuse Dextran leakage into the parenchyma that makes up the vast majority of observed leakage

162   and rare large bursts of leakage. When we performed these same time lapse experiments at 5

163   dpf, we observed significantly less overall tracer accumulation in the brain parenchyma over the

164   course of the hour in addition to reduced rates of tracer accumulation (slope of 4.641e-5

7

165   intensity/sec; Video 3; p<0.001, Mann-Whitney test; Figure 2B, 2D and 2E). Furthermore, 5 dpf

166   fish never exhibited bursts of tracer leakage as observed at 3 dpf. Overall, 5 dpf fish had far fewer

167   parenchymal cells filling with Dextran than at 3 dpf, as observed in the static tracer leakage assays

168   (Figure 1). We interpret these data to suggest that at early stages, most tracer leakage occurs

169   broadly through vessel walls potentially via unrestricted transcytosis with an occasional transient

170   rupture to endothelial integrity that lead to these large bursts of leakage. Once tracer is leaked

171   into the intercellular space of the parenchyma it is taken up by select parenchymal cells. As the

172   BBB matures both sources of leakage sharply decrease.

173

174   *Suppression of Transcytosis Governs BBB Development*

175   Given the observed differences in permeability during larval development, we next sought to

176   determine the subcellular mechanisms underlying the development of a functional BBB.

177   Therefore, we assessed BBB properties by performing intracardiac injections of electron-dense

178   NHS-gold nanoparticles (5 nm) followed by transmission electron microscopy (TEM) at different

179   developmental stages when the midbrain barrier is leaky (3 dpf) and when it is functionally sealed

180   to fluorescent tracers (5 and 7 dpf; Figure 3). All of the blood vessels analyzed had a maximal

181   diameter of 5 µm to enrich for capillaries and small veins. At 3 dpf, we found blood vessels in

182   direct contact with neurons and pericytes, with the pericytes sharing the endothelial basement

183   membrane (Figure 3A), as in the mammalian neurovascular unit. During this leaky developmental

184   stage, the endothelial basement membrane was filled with the electron-dense gold nanoparticles

185   (Figure 3A and 3B; turquoise arrowheads) with an average gold intensity of 1.29 ± 0.07 (luminal

186   gold intensity normalized to 1.0; Figure 3G), further demonstrating that the BBB is immature at 3

187   dpf. To decipher how the gold nanoparticles traverse from the lumen to the basement membrane,

188   we first looked at the tight junctions to see if the nanoparticles passed between apposed

189   endothelial cells. After careful examination, we observed that the nanoparticles were halted at the

190   "kissing points" between endothelial cells, indicating that tight junctions were functional prior to

191   formation of a functional BBB (49/49 functional tight junctions; Figure 3B; green arrowhead). As

192   transcytosis has been implicated in the maturation of the blood-retinal barrier (Chow and Gu,

193   2017), we next examined the levels of luminal and abluminal flask-shaped vesicles filled with gold

194   nanoparticles as a means of assessing transcytosis. Quantification of gold-filled luminal and

195   abluminal flask-shaped vesicles revealed an average of 0.21 ± 0.03 and 0.17 ± 0.02 vesicles/μm,

196   respectively (Figure 3H and 3I). These data reveal that the basement membrane becomes filled

197   with gold nanoparticles via vesicular transport rather than intercellular passage between immature

198   tight junctions.

199

200   When we repeated this assay at 5 dpf, when the barrier becomes less permeable to fluorescently

201   conjugated tracers (Figures 1 and 2), we still observe close contacts between endothelial cells

202   and pericytes (Figure 3C). At 5 dpf, the basement membrane was noticeably lacking gold particles

203   as compared to 3 dpf (Figure 3D), with a reduced average gold intensity of 0.85 ± 0.02 (Figure

204   3G). Like at 3 dpf, the tight junctions remained functional at 5 dpf, based on their capacity to halt

205   gold nanoparticles at the kissing points between neighboring endothelial cells (76/76 functional

206   tight junctions; Figure 3D). However, the levels of vesicles both luminally and abluminally were

207   notably decreased to 0.08 ± 0.01 and 0.07 ± 0.01 vesicles/μm, respectively (p<0.001 (luminal)

208   and p<0.0001 (abluminal), nested one-way ANOVA; Figure 3H and 3I). At 7 dpf the neurovascular

209   cellular interactions remained constant with endothelial cells in close contact with pericytes and

210   neurons, and with an unfilled basement membrane (average gold intensity of 0.91 ± 0.02; Figure

211   3E and 3G). Importantly, the tight junctions remained functional (51/51 functional tight junctions),

212   and the low vesicular densities observed at 5 dpf remained comparably low at 7 dpf with $0.07 \pm$

213   0.01 vesicles/μm, both luminally and abluminally (Figure 3F, 3H and 3I). Taken together with the

214   fluorescent tracer data, our data suggests that the zebrafish BBB becomes functional at 5 dpf via

215   suppression of vesicular trafficking.

216

217   *Conserved Role of Mfsd2a in Determining BBB Function*

218   Given the important role of suppressing transcytosis in determining the developmental maturation

219   of the zebrafish BBB, we wondered whether the key mammalian barrier regulator Mfsd2a, which

220   suppresses caveolae mediated transcytosis (Ben-Zvi et al., 2014; Andreone et al., 2017), plays a

221   conserved role in zebrafish. Zebrafish contain two paralogues of *Mfsd2a*, *mfsd2aa* and *mfsd2ab*.

222   *Mfsd2aa* is 61% identical to human *MFSD2A* and 62% identical to mouse *Mfsd2a* (Figure 4 –

223   Supplement 1A). *Mfsd2ab*, on the other hand, is 64% identical to human *MFSD2A* and mouse

224   *Mfsd2a* (Figure 4 – Supplement 1A). The two paralogues are only 68% identical to each other,

225   but they both contain the lipid binding domain that is critical for governing barrier properties (Figure

226   4 – Supplement 1A; Andreone et al., 2017). Given the lack of a clear paralogue that most closely

227   resembles *Mfsd2a*, we generated CRISPR mutants for both paralogues independently.

228   *Mfsd2aa*$^{hm37/hm37}$ mutants have a 7 bp deletion in exon 2 (Figure 4 – Supplement 1B) that is

229   predicted to lead to a premature stop codon at amino acid 82 (Figure 4 – Supplement 1A; black

230   box). Homozygous *mfsd2aa* mutants are viable and fertile. *Mfsd2ab*$^{hm38/hm38}$ mutants have a 19

231   bp deletion in exon 5 (Figure 4 – Supplement 1B) that is predicted to lead to a premature stop

232   codon at amino acid 175 (Figure 4 – Supplement 1A; black box). Homozygous *mfsd2ab* mutants

233   are also viable and fertile. Neither mutant displayed obvious angiogenic defects, similar to the

234   normal vasculature observed in mouse *Mfsd2a* mutants (Ben-Zvi et al., 2014).

235

236   To investigate whether either paralogue was necessary for barrier formation, we performed NHS

237   tracer injection assays as we did to identify the developmental timeline of barrier formation and

238   assayed for midbrain leakage at 5 dpf. In addition to the use of the exogenous injected fluorescent

239   tracer (1 kDa NHS), we also assayed the leakage of the endogenous transgenic serum DBP-

240   EGFP fusion protein (Tg(*l-fabp:DBP-EGFP*)). *Mfsd2aa* mutants displayed about a two-fold

241   increase in midbrain tracer-containing parenchymal cells, both for the injected 1 kDa NHS and

242   the endogenous serum transgene 80 kDa DBP-EGFP, at 5 dpf compared to wildtype sibling

243   controls (Figure 4). These data suggest that mfsd2aa plays a similar role to mouse Mfsd2a in

244   determining barrier properties. Conversely, *mfsd2ab* mutants displayed similarly low levels of

245   tracer-containing parenchymal cells to wildtype controls at 5 dpf in the midbrain (Figure 4 -

246   Supplement 2), indicating that mfsd2ab is dispensable for functional barrier formation. To see if

247   the loss of both paralogues resulted in increased barrier permeability, we investigated

248   *mfsd2aa^{hm37/hm37}; mfsd2ab^{hm38/hm38}* double mutants for BBB permeability using the endogenous

249   serum DBP-EGFP fusion protein (Figure 4 - Supplement 3). While *mfsd2aa* single mutants

250   displayed the previously observed increase in barrier permeability and *mfsd2ab* single mutants

251   did not, *mfsd2aa^{hm37/hm37}; mfsd2ab^{hm38/hm38}* double mutants displayed similar levels of increased

252   barrier permeability to the *mfsd2aa* single mutants (Figure 4 - Supplement 3). Taken together,

253   these data suggest that the two paralogues, while structurally similar, play different roles, with

254   zebrafish mfsd2aa and mammalian Mfsd2a sharing a conserved role in determining barrier

255   permeability.

256

257   Given the leakage phenotype in *mfsd2aa* mutants at 5 dpf, we next wanted to examine whether

258   the leakage phenotype persisted into adulthood. To address this, we performed retro-orbital

259   injections of HRP, which has been shown to be confined within the adult zebrafish brain

260   vasculature (Jeong et al., 2008), and allowed the HRP to circulate for 30 minutes. As expected,

261   the wildtype siblings retained the HRP within their blood vessels (Figure 5A). However, *mfsd2aa*

262   mutants exhibited HRP extravasation into the brain parenchyma (Figure 5B), suggesting that the

263   leakage phenotype was not limited to larval fish. Finally, to determine whether this increased

264   permeability was due to increased transcytosis as in *Mfsd2a* knockout mice, we measured

265   vesicular density in capillaries with luminal diameters less than 5 μm from adult mutant and

266   wildtype siblings using TEM. The *mfsd2aa* mutant blood vessels appeared morphologically

267   normal by TEM, composed of a thin single layer of endothelial cells in close contact with pericytes,

268   as observed in their wildtype siblings (Figure 5C and 5D). A closer examination of the endothelial

269   cells revealed electron-dense tight junction complexes between all apposed endothelial cells in

270   both wildtype and *mfsd2aa* mutant fish (Figure 5E and 5F). However, while wildtype fish display

271   similarly low levels of luminal (0.1 vesicles/μm) and abluminal (0.11 vesicles/μm) vesicular

272   densities to those observed at 7 dpf (Figure 5E- 5H), *mfsd2aa* mutant fish display a significant

273   increase in luminal and abluminal vesicular densities (0.29 and 0.27 vesicles/μm, respectively)

274   compared to wildtype siblings (Figure 5E-5H). Interestingly this increase in vesicular abundance

275   is even higher than that observed during early barrier development at 3 dpf (Figure 2). These data

276   also suggest that the increased tracer leakage observed in *mfsd2aa* mutants results from an

277   increase in vesicular trafficking across the BBB, further supporting a conserved role for mfsd2aa

278   in determining barrier properties. In contrast to *mfsd2aa* mutants, *mfsd2ab* mutants displayed

279   similar levels of abluminal and luminal vesicular pit density to wildtype siblings (Figure 5 -

280   Supplement 1), further demonstrating that the paralog *mfsd2ab* does not play a conserved role in

281   determining barrier properties in zebrafish.

282

283   **Discussion**

284   One of the major advantages to studying the BBB in zebrafish is the ability to perform live imaging

285   of tracer permeability dynamics. We provide some of the first data on the dynamics of immature

286   barrier leakage. At 3 dpf, we observed two types of leakage, the gradual overall increase in the

287   parenchyma and rare transient bursts, both from a migrating sprout and established blood

288   vessels. We attribute the gradual diffuse increase in parenchymal tracer uptake to the high levels

289   of vesicular trafficking observed in our TEM analyses in which the endothelial basement

290   membrane became filled with gold nanoparticles. Therefore, the parenchymal Dextran intensity

291   measurements provide a direct proxy for the rates of BBB transcytosis *in vivo*. The rarer bursts of

292   leakage, on the other hand, could be due to fleeting tight junctional ruptures between neighboring

293   endothelial cells rather than increased vesicular trafficking. As these events were extremely

294   scarce during our time lapse imaging, it would be nearly impossible to capture these potential

12

295   junctional breaches by TEM to confirm this hypothesis. However, with continuing advances in the

296   resolution of fluorescence microscopy, we could use zebrafish to resolve whether these two types

297   of leakage, gradual and bursting, proceed through the same or different subcellular routes into

298   the brain parenchyma, either paracellularly or transcellularly.

299

300   Among the various clathrin-independent transcytotic pathways (Tuma and Hubbard, 2003;

301   Sandvig et al., 2018), caveolae are particularly abundant in vascular endothelial cells (Frank et

302   al., 2003). Caveolae are caveolin-coated 50-100 nm flask-shaped invaginations of the plasma

303   membrane (Palade, 1953; Palade, 1961). Furthermore, the suppression of caveolae-mediated

304   transcytosis regulates the development and function of both the mouse blood-retinal barrier and

305   the BBB (Andreone et al., 2017; Chow and Gu, 2017). Taken together, this suggests that the

306   increased transcytosis during early larval stages is most likely caveolae mediated. Interestingly,

307   the linear profile of Dextran uptake in the midbrain at 3 dpf closely resembles the caveolae-

308   mediated uptake of a fluorescently-conjugated aminopeptidase P (APP) antibody in the mouse

309   lung (Oh et al., 2007). While similarly linear, the scale is on the order of minutes in the larval

310   zebrafish brain versus seconds in the mouse lung. This discrepancy in timing is most likely due

311   to the large difference in the vesicular densities between the immature BBB endothelium (average

312   of 2 vesicles/μm^2) and the continuous endothelium of peripheral tissues, which ranges from 30 to

313   98 vesicles/μm^2 on the luminal membrane of diaphragm and myocardial endothelium (Simionescu

314   et al., 1974). Since loss of caveolin 1 is sufficient to precociously seal the blood-retinal barrier at

315   the angiogenic front (Chow and Gu, 2017), it would be interesting in future work to examine

316   whether zebrafish caveolin 1 mutants (Cao et al., 2016), which are viable as homozygotes, also

317   exhibit an earlier onset of BBB maturation.

318

319   BBB permeability is tightly regulated by endothelial cell interactions with pericytes and astroglial

320   cells. For the first time, we visualized their locations under TEM in zebrafish throughout barrier

13

321 development. Pericytes have been shown to be essential for establishing the mammalian BBB

322 (Armulik et al., 2010; Bell et al., 2010; Daneman et al., 2010). Similarly, pericyte deficient

323 notch3[fh332] fish display increased BBB permeability in a tight junction independent manner like

324 pericyte-deficient mice (Wang et al., 2014). Our TEM data show that zebrafish pericytes are in

325 close contact with brain endothelial cells (Figures 2 and 5), even at the earliest stage examined

326 (3 dpf; Figure 2), and are embedded within the endothelial basement membrane as in mammals.

327 Our subcellular localization data is in line with a growing body of evidence for the conserved role

328 of pericytes in the zebrafish BBB (Wang et al., 2014; Lei et al., 2017). While zebrafish lack stellate

329 astrocytes, they possess radial glia that express several astrocytic markers, such as Gfap,

330 glutamine synthetase (GS), and Aqp4 (Jeong et al., 2008; Grupp et al., 2010). Previous studies

331 have disagreed on the extent of radial glia interactions with BBB endothelial cells in zebrafish.

332 Some studies report glia-BBB interactions that are similar to those observed in mammals (Jeong

333 et al., 2008), while others report little to no interaction (Grupp et al., 2010). Our TEM data in adult

334 zebrafish do not find a necessity for glial interactions with the brain vasculature, with endothelial

335 cells occasionally in contact with electron-light glia (Figure 5B), but often not (Figure 5A). This

336 appears to be a unique feature of the zebrafish BBB and should be considered carefully when

337 using zebrafish as a model system for the BBB.

338

339 Taken together this study provides a thorough characterization of the development of the

340 zebrafish BBB, highlighting regional differences in timing of maturation and capturing the

341 dynamics of the immature BBB. Furthermore, our developmental TEM series provides the first

342 direct evidence of vesicular trafficking regulating zebrafish BBB development. Finally, we have

343 shown that this down-regulation of vesicular trafficking is necessary for BBB formation, as

344 *mfsd2aa* mutants display increased barrier permeability due to unsuppressed transcytosis. We

345 hope that this work will serve as a launching pad for future studies using zebrafish to understand

346 the molecular regulators of BBB development and homeostasis in vertebrates.

14

Author Contributions

N.M.O., S.G.M. and C.G. conceived the project and designed experiments. N.M.O. performed all experiments and analyzed all data. N.M.O., S.G.M. and C.G wrote the manuscript.

Materials and Methods

Zebrafish Strains and Maintenance

Zebrafish were maintained at 28.5°C following standard protocols (Westerfield, 1993). All zebrafish work was approved by the Harvard Medical Area Standing Committee on Animals under protocol number 04487. Adult fish were maintained on a standard light-dark cycle from 9 am to 11 pm. Adult fish, age 3 months to 2 years, were crossed to produce embryos and larvae. These studies used the AB wildtype strain and the transgenic strains Tg(*l-fabp:DBP-EGFP),* Tg(*kdrl:mCherry*), and Tg(*kdrl:HRAS-mCherry*).

Tracer Injections

Larvae were immobilized with tricaine and placed in an agarose injection mold with their hearts facing upwards. 2.3 nl of Alexa Fluor 405 NHS Ester (Thermo Fisher: A30000) or Alexa Fluor 647 10 kDa Dextran (Thermo Fisher:D22914) fluorescently conjugated tracers (10 mg/ml) were injected into the cardiac sac using Nanoject II (Drummond Scientific, Broomall, PA). Embryos were then mounted with 1.5% low gelling agarose (Sigma: A9414) in embryo water on 0.17 mm coverslips and imaged live within 2 hours post injection. For developmental electron microscopy experiments, 2.3 nl of 5 nm NHS-activated gold nanoparticles (Cytodiagnostics: CGN5K-5-1, ~1.1^{14} particles/ml in PBS) were injected into the cardiac sac just as for the fluorescently conjugated tracers. After 5 minutes of circulation, the fish were fixed for electron microscopy. Adults were briefly immobilized with tricaine and retroorbitally injected with 3 µl of HRP (2 mg/ml dissolved in PBS) using a 10 µl Hamilton syringe. After 30 minutes of HRP circulation, the brains were fixed in 4% PFA overnight at 4C. Following fixation the brains were washed three times and sectioned coronally with a vibratome (50 µm). Sections were then stained at room temperature in 0.05 M Tris-HCl pH 7.6 buffer containing 0.5 mg/ml 3-39 diaminobenzidine (DAB, Sigma Aldrich) and 0.01% hydrogen peroxide.

Transmission Electron Microscopy (TEM)

Fish were anesthetized with tricaine and initially fixed by immersion in 4% paraformaldehyde (VWR:15713-S) /0.1M sodium-cacodylate (VWR:11653). Following this initial fixation, the larval fish and adults with exposed brains were further fixed for 7-14 days in 2% glutaraldehyde (Electron Microscopy Sciences: 16320)/ 4% paraformaldehyde/ 0.1M sodium-cacodylate at room temperature. Following fixation, larvae or dissected brains were washed overnight in 0.1M sodium-cacodylate. Entire larval heads or coronal vibratome free-floating sections of adult brains (50 µm) were post-fixed in 1% osmium tetroxide and 1.5% potassium ferrocyanide, dehydrated, and embedded in epoxy resin. Ultrathin sections of 80 nm were then cut from the block surface and collected on copper grids. The adult sections were counter-stained with Reynold's lead citrate prior to imaging.

CRISPR Mutants

Mfsd2aa mutant fish were generated by injection of Cas9 RNA and a single guide RNA (5'-GGTGTGTTTTGCGATCGGAG-3') targeting exon 3 into single-cell fertilized wildtype embryos. *Mfsd2ab* mutant fish were generated by injection of Cas9 protein and a single guide RNA (5'-TGAGAGCAGAGTAGGGCACG-3') targeting exon 5 into single-cell fertilized double transgenic Tg(*l-fabp:DBP-EGFP; kdrl:mCherry)* embryos. F0 injected fish were raised, outcrossed to wildtype fish and screened for potential mutant founders by PCR and sequencing. The stable *mfsd2aa* mutant line was genotyped using 5'-AAATCACCTCTTCCAGTGAGGA-3' and 5'-ATAGTAACAAAACGATGCTGAGCC-3' primers. *Mfsd2ab* mutants were genotyped using 5'-GTCTACTCCATTTGCTGTACTTTGC-3' and 5'-CAGGTCAATCTCAGTGCTGATACAG-3' primers.

Imaging

All live imaging of tracer permeability was performed on a Leica SP8 laser scanning confocal microscope. Time lapse imaging was performed on the SP8 using a resonance scanner. A 1200EX electron microscope (JOEL) equipped with a 2k CCD digital camera (AMT) was used for all TEM studies. Images were visualized and quantified using ImageJ (NIH) and Adobe Photoshop. Time lapse videos were visualized as 3D reconstructions and cropped to highlight particular blood vessels of interest using Imaris software (Bitplane).

Tracer Permeability Quantification

All quantification was performed on blinded image sets. Parenchymal cells containing injected tracers outside of the blood vessels were manually counted throughout z-stacks that spanned the entire larval brain in depth. Z-stacks were collected with 0.59 µm z-steps using a 25x water immersion objective on a Leica SP8 laser scanning confocal microscope. The Dextran intensity was measured in six parenchymal regions of average intensity projections of the time lapse videos and averaged as a single value per fish. These values were normalized to the average fluorescence intensity in the lumen at each time point.

TEM Quantification

For all TEM quantifications, vesicular density values were calculated from the number of non-clathrin coated flask-shaped vesicles per µm of endothelial luminal or abluminal membrane for each image collected. Embryonic basement membrane gold intensity was measured in three regions per endothelial cell and normalized to luminal gold intensity values within individual images using ImageJ. All images for analysis were collected at 12000x magnification on the JOEL 1200EX electron microscope. 10-15 vessels were quantified for each fish, with each color representing a different fish.

18

438   **Statistical Analysis**

439   All statistical analyses were performed using Prism 8 (GraphPad Software). Two group

440   comparisons were analyzed using an unpaired two-tailed t test. Nested t tests were employed for

441   all electron microscopy comparisons to account for the actual N versus vessels analyzed. Multiple

442   group comparisons were analyzed with one-way ANOVA, followed by a post hoc Tukey's multiple

443   comparison test. The time lapse leakage dynamics were analyzed with a Mann-Whitney U test to

444   discriminate whether the two patterns of leakage accumulation were different. Sample size for all

445   experiments was determined empirically using standards generally employed by the field, and no

446   data was excluded when performing statistical analysis. Standard error of the mean was

447   calculated for all experiments and displayed as errors bars in graphs. Statistical details for specific

448   experiments, including exact n values and what n represents, precision measures, statistical tests

449   used, and definitions of significance can be found in the Figure Legends.

450

451 Ablain, J., Durand, E.M., Yang, S., Zhou, Y., and Zon, L.I. 2015. A CRISPR/Cas9 Vector System
452   for Tissue-Specific Gene Disruption in Zebrafish. Dev. Cell **32**(6): 756–764. Elsevier Inc.
453   doi:10.1016/j.devcel.2015.01.032.
454 Albadri, S., Del Bene, F., and Revenu, C. 2017. Genome editing using CRISPR/Cas9-based
455   knock-in approaches in zebrafish. Methods **121-122**: 77–85. Elsevier Inc.
456   doi:10.1016/j.ymeth.2017.03.005.
457 Andreone, B.J., Chow, B.W., Tata, A., Lacoste, B., Ben-Zvi, A., Bullock, K., Deik, A.A., Ginty,
458   D.D., Clish, C.B., and Gu, C. 2017. Blood-Brain Barrier Permeability Is Regulated by Lipid
459   Transport-Dependent Suppression of Caveolae-Mediated Transcytosis. Neuron **94**(3): 581–
460   594.e5. doi:10.1016/j.neuron.2017.03.043.
461 Andreone, B.J., Lacoste, B., and Gu, C. 2015. Neuronal and Vascular Interactions.
462   http://dx.doi.org.ezp-prod1.hul.harvard.edu/10.1146/annurev-neuro-071714-033835. Annual
463   Reviews. doi:10.1146/annurev-neuro-071714-033835.
464 Armer, H.E.J., Mariggi, G., Png, K.M.Y., Genoud, C., Monteith, A.G., Bushby, A.J., Gerhardt, H.,
465   and Collinson, L.M. 2009. Imaging Transient Blood Vessel Fusion Events in Zebrafish by
466   Correlative Volume Electron Microscopy. PLoS ONE **4**(11): e7716–10.
467   doi:10.1371/journal.pone.0007716.
468 Armulik, A., Genové, G., Mäe, M., Nisancioglu, M.H., Wallgard, E., Niaudet, C., He, L., Norlin, J.,
469   Lindblom, P., Strittmatter, K., Johansson, B.R., and Betsholtz, C. 2010. Pericytes regulate the
470   blood-brain barrier. Nature **468**(7323): 557–561. doi:10.1038/nature09522.
471 Bell, R.D., Winkler, E.A., Sagare, A.P., Singh, I., LaRue, B., Deane, R., and Zlokovic, B.V. 2010b.
472   Pericytes control key neurovascular functions and neuronal phenotype in the adult brain and
473   during brain aging. Neuron **68**(3): 409–427. doi:10.1016/j.neuron.2010.09.043.
474 Ben-Zvi, A., Lacoste, B., Kur, E., Andreone, B.J., Mayshar, Y., Yan, H., and Gu, C. 2014. Mfsd2a
475   is critical for the formation and function of the blood-brain barrier. Nature **509**(7501): 507–
476   511. doi:10.1038/nature13324.
477 Brightman, M.W., and Reese, T.S. 1969. Junctions between intimately apposed cell membranes
478   in the vertebrate brain. J. Cell Biol. **40**(3): 648–677.
479 Campbell, M., Kiang, A.-S., Kenna, P.F., Kerskens, C., Blau, C., O'Dwyer, L., Tivnan, A., Kelly,
480   J.A., Brankin, B., Farrar, G.-J., and Humphries, P. 2008. RNAi-mediated reversible opening
481   of the blood-brain barrier. J. Gene Med. **10**(8): 930–947. doi:10.1002/jgm.1211.
482 Cao, J., Navis, A., Ben D Cox, Dickson, A.L., Gemberling, M., Karra, R., Bagnat, M., and Poss,
483   K.D. 2016. Single epicardial cell transcriptome sequencing identifies Caveolin 1 as an
484   essential factor in zebrafish heart regeneration. Development **143**(2): 232–243. Oxford
485   University Press for The Company of Biologists Limited. doi:10.1242/dev.130534.
486 Chow, B.W., and Gu, C. 2017. Gradual Suppression of Transcytosis Governs Functional Blood-
487   Retinal Barrier Formation. Neuron **93**(6): 1325–1333.e3. Elsevier Inc.
488   doi:10.1016/j.neuron.2017.02.043.
489 Daneman, R., Zhou, L., Kebede, A.A., and Barres, B.A. 2010. Pericytes are required for blood-
490   brain barrier integrity during embryogenesis. Nature **468**(7323): 562–566.
491   doi:10.1038/nature09513.
492 Fleming, A., Diekmann, H., and Goldsmith, P. 2013. Functional characterisation of the maturation
493   of the blood-brain barrier in larval zebrafish. PLoS ONE **8**(10): e77548.
494   doi:10.1371/journal.pone.0077548.
495 Franco, C.A., Jones, M.L., Bernabeu, M.O., Geudens, I., Mathivet, T., Rosa, A., Lopes, F.M.,
496   Lima, A.P., Ragab, A., Collins, R.T., Phng, L.-K., Coveney, P.V., and Gerhardt, H. 2015.
497   Dynamic Endothelial Cell Rearrangements Drive Developmental Vessel Regression. PLoS
498   Biol. **13**(4): e1002125–19. doi:10.1371/journal.pbio.1002125.
499 Frank, P.G., Woodman, S.E., Park, D.S., and Lisanti, M.P. 2003. Caveolin, Caveolae, and
500   Endothelial Cell Function. Arterioscler. Thromb. Vasc. Biol. **23**(7): 1161–1168.
501   doi:10.1161/01.ATV.0000070546.16946.3A.

Gagnon, J.A., Valen, E., Thyme, S.B., Huang, P., Ahkmetova, L., Pauli, A., Montague, T.G., Zimmerman, S., Richter, C., and Schier, A.F. 2014. Efficient Mutagenesis by Cas9 Protein-Mediated Oligonucleotide Insertion and Large-Scale Assessment of Single-Guide RNAs. PLoS ONE **9**(5): e98186–8. doi:10.1371/journal.pone.0098186.

Galanternik, M.V., Castranova, D., Gore, A.V., Blewett, N.H., Jung, H.M., Stratman, A.N., Kirby, M.R., Iben, J., Miller, M.F., Kawakami, K., Maraia, R.J., and Weinstein, B.M. 2017. A novel perivascular cell population in the zebrafish brain. Elife **6**: 45. doi:10.7554/eLife.24369.

Geudens, I., Coxam, B., Alt, S., Gebala, V., Vion, A.-C., Rosa, A., and Gerhardt, H. 2018. Arterio-Venous Remodeling in the Zebrafish Trunk Is Controlled by Genetic Programming and Flow-Mediated Fine-Tuning. : 1–32. doi:10.1101/403550.

Geudens, I., Herpers, R., Hermans, K., Segura, I., Ruiz de Almodovar, C., Bussmann, J., De Smet, F., Vandevelde, W., Hogan, B.M., Siekmann, A., Claes, F., Moore, J.C., Pistocchi, A.S., Loges, S., Mazzone, M., Mariggi, G., Bruyère, F., Cotelli, F., Kerjaschki, D., Noël, A., Foidart, J.-M., Gerhardt, H., Ny, A., Langenberg, T., Lawson, N.D., Duckers, H.J., Schulte-Merker, S., Carmeliet, P., and Dewerchin, M. 2010. Role of Delta-like-4/Notch in the Formation and Wiring of the Lymphatic Network in Zebrafish. Arterioscler. Thromb. Vasc. Biol. **30**(9): 1695–1702. doi:10.1161/ATVBAHA.110.203034.

Grupp, L., Wolburg, H., and Mack, A.F. 2010. Astroglial structures in the zebrafish brain. Journal of Comparative Neurology **518**(21): 4277–4287. Wiley Subscription Services, Inc., A Wiley Company. doi:10.1002/cne.22481.

Guemez-Gamboa, A., Nguyen, L.N., Yang, H., Zaki, M.S., Kara, M., Ben-Omran, T., Akizu, N., Rosti, R.O., Rosti, B., Scott, E., Schroth, J., Copeland, B., Vaux, K.K., Cazenave-Gassiot, A., Quek, D.Q.Y., Wong, B.H., Tan, B.C., Wenk, M.R., Gunel, M., Gabriel, S., Chi, N.C., Silver, D.L., and Gleeson, J.G. 2015. Inactivating mutations in MFSD2A, required for omega-3 fatty acid transport in brain, cause a lethal microcephaly syndrome. Nat. Genet. **47**(7): 809–813. doi:10.1038/ng.3311.

Harel, T., Quek, D.Q.Y., Wong, B.H., Cazenave-Gassiot, A., Wenk, M.R., Fan, H., Berger, I., Shmueli, D., Shaag, A., Silver, D.L., Elpeleg, O., and Edvardson, S. 2018. Homozygous mutation in MFSD2A, encoding a lysolipid transporter for docosahexanoic acid, is associated with microcephaly and hypomyelination. Neurogenetics **19**(4): 227-235. doi:10.1007/s10048-018-0556-6.

Herbert, S.P., Cheung, J.Y.M., and Stainier, D.Y.R. 2012. Determination of Endothelial Stalk versus Tip Cell Potential during Angiogenesis by H2.0-like Homeobox-1. Current Biology **22**(19): 1789–1794. Elsevier Ltd. doi:10.1016/j.cub.2012.07.037.

Herbert, S.P., Huisken, J., Kim, T.N., Feldman, M.E., Houseman, B.T., Wang, R.A., Shokat, K.M., and Stainier, D.Y.R. 2009. Arterial-venous segregation by selective cell sprouting: an alternative mode of blood vessel formation. Science **326**(5950): 294–298. doi:10.1126/science.1178577.

Hogan, B.M., and Schulte-Merker, S. 2017. How to Plumb a Pisces: Understanding Vascular Development and Disease Using Zebrafish Embryos. Dev. Cell **42**(6): 567–583. Elsevier. doi:10.1016/j.devcel.2017.08.015.

Hwang, W.Y., Fu, Y., Reyon, D., Maeder, M.L., Tsai, S.Q., Sander, J.D., Peterson, R.T., Yeh, J.-R.J., and Joung, J.K. 2013. Efficient genome editing in zebrafish using a CRISPR-Cas system. Nat. Biotechnol. **31**(3): 227–229. doi:10.1038/nbt.2501.

Janzer, R.C., and Raff, M.C. 1987. Astrocytes induce blood-brain barrier properties in endothelial cells. Nature **325**(6101): 253–257. doi:10.1038/325253a0.

Jin, S.-W., Beis, D., Mitchell, T., Chen, J.-N., and Stainier, D.Y.R. 2005. Cellular and molecular analyses of vascular tube and lumen formation in zebrafish. Development **132**(23): 5199–5209. The Company of Biologists Ltd. doi:10.1242/dev.02087.

551 Jeong, J.-Y., Kwon, H.-B., Ahn, J.-C., Kang, D., Kwon, S.-H., Park, J.A., and Kim, K.-W. 2008.
552   Functional and developmental analysis of the blood–brain barrier in zebrafish. Brain Res.
553   Bull. **75**(5): 619–628. doi:10.1016/j.brainresbull.2007.10.043.
554 Lawson, N.D., and Weinstein, B.M. 2002. In Vivo Imaging of Embryonic Vascular Development
555   Using Transgenic Zebrafish. Dev. Biol. **248**(2): 307–318. doi:10.1006/dbio.2002.0711.
556 Lei, D., Jin, X., Wen, L., Dai, H., Ye, Z., and Wang, G. 2017. bmp3 is Required for Integrity of
557   Blood Brain Barrier by Promoting Pericyte Coverage in Zebrafish Embryos. *Current Molecular*
558   *Medicine*, *17*(4).
559 Matsuoka, R.L., Marass, M., Avdesh, A., Helker, C.S., Maischein, H.-M., Grosse, A.S., Kaur, H.,
560   Lawson, N.D., Herzog, W., and Stainier, D.Y. 2016. Radial glia regulate vascular patterning
561   around the developing spinal cord. Elife **5**: 1328. doi:10.7554/eLife.20253.
562 Nitta, T., Hata, M., Gotoh, S., Seo, Y., Sasaki, H., Hashimoto, N., Furuse, M., and Tsukita, S.
563   2003. Size-selective loosening of the blood-brain barrier in claudin-5-deficient mice. J. Cell
564   Biol. **161**(3): 653–660. Rockefeller University Press. doi:10.1083/jcb.200302070.
565 O'Brown, N.M., Pfau, S.J., and Gu, C. 2018. Bridging barriers: a comparative look at the blood–
566   brain barrier across organisms. **32**(7-8): 466–478. doi:10.1101/gad.309823.117.
567 Oh, P., Borgström, P., Witkiewicz, H., Li, Y., Borgström, B.J., Chrastina, A., Iwata, K., Zinn, K.R.,
568   Baldwin, R., Testa, J.E., and Schnitzer, J.E. 2007. Live dynamic imaging of caveolae pumping
569   targeted antibody rapidly and specifically across endothelium in the lung. Nat. Biotechnol.
570   **25**(3): 327–337. doi:10.1038/nbt1292.
571 Palade, G.E. 1953. Fine structure of blood capillaries. J. Appl. Phys. **24**: 1424.
572 Palade, G.E. 1961. Blood capillaries of the heart and other organs. Circulation **24**: 368–388.
573 Phng, L.-K., Potente, M., Leslie, J.D., Babbage, J., Nyqvist, D., Lobov, I., Ondr, J.K., Rao, S.,
574   Lang, R.A., Thurston, G., and Gerhardt, H. 2009. Nrarp Coordinates Endothelial Notch and
575   Wnt Signaling to Control Vessel Density in Angiogenesis. Dev. Cell **16**(1): 70–82. Elsevier.
576   doi:10.1016/j.devcel.2008.12.009.
577 Quiñonez-Silvero, C., Hübner, K., and Herzog, W. 2019. Development of the brain vasculature
578   and the blood-brain barrier in zebrafish. Dev. Biol.: 1–34. Elsevier Inc.
579   doi:10.1016/j.ydbio.2019.03.005.
580 Reese, T.S., and Karnovsky, M.J. 1967. Fine structural localization of a blood-brain barrier to
581   exogenous peroxidase. J. Cell Biol. **34**(1): 207–217. The Rockefeller University Press.
582 Sanchez-Covarrubias, L., Slosky, L.M., Thompson, B.J., Davis, T.P., and Ronaldson, P.T. 2014.
583   Transporters at CNS barrier sites: obstacles or opportunities for drug delivery? Curr. Pharm.
584   Des. **20**(10): 1422–1449.
585 Sandvig, K., Kavaliauskiene, S., and Skotland, T. 2018. Clathrin-independent endocytosis: an
586   increasing degree of complexity. Histochem. Cell Biol. **150**(2): 107–118. doi:10.1007/s00418-
587   018-1678-5.
588 Santoro, M.M., Samuel, T., Mitchell, T., Reed, J.C., and Stainier, D.Y.R. 2007. Birc2 (cIap1)
589   regulates endothelial cell integrity and blood vessel homeostasis. Nat. Genet. **39**(11): 1397–
590   1402. doi:10.1038/ng.2007.8.
591 Simionescu, M., Simionescu, N., and Palade, G.E. 1974. Morphometric data on the endothelium
592   of blood capillaries. J. Cell Biol. **60**(1): 128–152. Rockefeller University Press.
593   doi:10.1083/jcb.60.1.128.
594 Sohet, F., Lin, C., Munji, R.N., Lee, S.Y., Ruderisch, N., Soung, A., Arnold, T.D., Derugin, N.,
595   Vexler, Z.S., Yen, F.T., and Daneman, R. 2015. LSR/angulin-1 is a tricellular tight junction
596   protein involved in blood-brain barrier formation. J. Cell Biol. **208**(6): 703–711. Rockefeller
597   University Press. doi:10.1083/jcb.201410131.
598 Stratman, A.N., Pezoa, S.A., Farrelly, O.M., Castranova, D., Dye, L.E., III, Butler, M.G., Sidik, H.,
599   Talbot, W.S., and Weinstein, B.M. 2017. Interactions between mural cells and endothelial
600   cells stabilize the developing zebrafish dorsal aorta. Development **144**(1): 115–127.
601   doi:10.1242/dev.143131.

Stewart, P.A., and Wiley, M.J. 1981. Developing nervous tissue induces formation of blood-brain barrier characteristics in invading endothelial cells: a study using quail--chick transplantation chimeras. Dev. Biol. **84**(1): 183–192.

Tuma, P.L., and Hubbard, A.L. 2003. Transcytosis: Crossing Cellular Barriers. Physiological Reviews **83**(3): 871–932. doi:10.1152/physrev.00001.2003.

Ulrich, F., Carretero-Ortega, J., Menéndez, J., Narvaez, C., Sun, B., Lancaster, E., Pershad, V., Trzaska, S., Véliz, E., Kamei, M., Prendergast, A., Kidd, K.R., Shaw, K.M., Castranova, D.A., Pham, V.N., Lo, B.D., Martin, B.L., Raible, D.W., Weinstein, B.M., and Torres-Vázquez, J. 2016. Reck enables cerebrovascular development by promoting canonical Wnt signaling. Development **143**(1): 147–159. doi:10.1242/dev.123059

Umans, R.A., Henson, H.E., Mu, F., Parupalli, C., Ju, B., Peters, J.L., Lanham, K.A., Plavicki, J.S., and Taylor, M.R. 2017. CNS angiogenesis and barriergenesis occur simultaneously. Dev. Biol. **425**(2): 101–108. doi:10.1016/j.ydbio.2017.03.017.

Vanhollebeke, B., Stone, O.A., Bostaille, N., Cho, C., Zhou, Y., Maquet, E., Gauquier, A., Cabochette, P., Fukuhara, S., Mochizuki, N., Nathans, J., and Stainier, D.Y. 2015. Tip cell-specific requirement for an atypical Gpr124- and Reck-dependent Wnt/β-catenin pathway during brain angiogenesis. Elife **4**. doi:10.7554/eLife.06489.

Varshney, G.K., Sood, R., and Burgess, S.M. 2015. Understanding and Editing the Zebrafish Genome. *In* Advances in Genetics. Elsevier Ltd. doi:10.1016/bs.adgen.2015.09.002.

Wang, Y., Pan, L., Moens, C.B., and Appel, B. 2014. Notch3 establishes brain vascular integrity by regulating pericyte number. Development **141**(2): 307–317. Oxford University Press for The Company of Biologists Limited. doi:10.1242/dev.096107.

Westerfield, M. 1993. The zebrafish book: a guide for the laboratory use of zebrafish (Brachydanio rerio).

Wilkinson, R.N., and van Eeden, F.J.M. 2014. The Zebrafish as a Model of Vascular Development and Disease. *In* Genetics of Cardiovascular Disease, 1st edition. Elsevier Inc. doi:10.1016/B978-0-12-386930-2.00005-7.

Xie, J., Farage, E., Sugimoto, M., and Anand-Apte, B. 2010. A novel transgenic zebrafish model for blood-brain and blood-retinal barrier development. BMC Dev. Biol. **10**: 76. doi:10.1186/1471-213X-10-76.

Yanagida, K., Liu, C.H., Faraco, G., Galvani, S., Smith, H.K., Burg, N., Anrather, J., Sanchez, T., Iadecola, C., and Hla, T. 2017. Size-selective opening of the blood–brain barrier by targeting endothelial sphingosine 1–phosphate receptor 1. Proc. Natl. Acad. Sci. U.S.A. **114**(17): 4531–4536. doi:10.1073/pnas.1618659114.

Zhao, Z., Nelson, A.R., Betsholtz, C., and Zlokovic, B.V. 2015. Establishment and Dysfunction of the Blood-Brain Barrier. Cell **163**(5): 1064–1078. doi:10.1016/j.cell.2015.10.067.

638
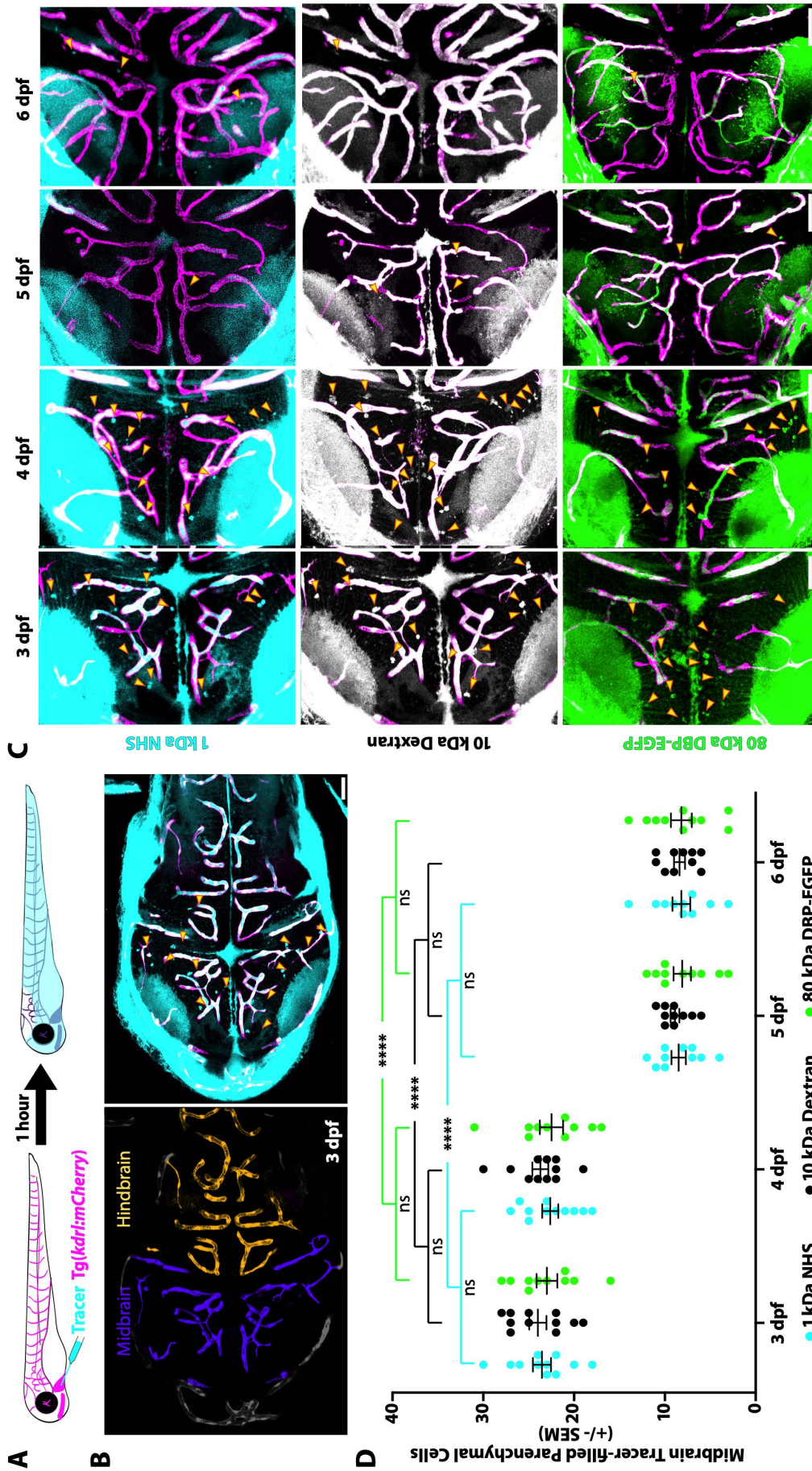
639 **Figure 1. The midbrain BBB becomes functional at 5 dpf.** (A) Diagram of the tracer leakage

640 assay. Fluorescently conjugated tracers (turquoise) were injected intracardially into transgenic

641 fish that express mCherry in the vasculature (magenta; Tg(*kdrl:mCherry*)) and allowed to circulate

642 for one hour before imaging. (B) Dorsal view maximum intensity projection of the larval brain

643 vasculature at 3 dpf. Left image is pseudo-colored to demarcate the midbrain (violet) and the

644 hindbrain (gold) vasculature. Right image shows the NHS tracer (turquoise) in the entire larval

645 brain, with a large number of tracer-filled parenchymal cells marked by yellow arrowheads in the

646 midbrain. (C) Representative dorsal view maximum intensity projections of larval zebrafish

647 midbrains at different developmental stages reveal increased permeability at 3 and 4 dpf

648 compared to 5 and 6 dpf. The increased early permeability was observed with two injected tracers

649 of different sizes, a 1 kDa NHS (turquoise) and a 10 kDa Dextran (white), as well with an 80 kDa

650 transgenic serum protein DBP-EGFP (green). Yellow arrowheads demarcate the tracer-filled

651 parenchymal cells outside of the vasculature (magenta). Scale bars represent 50 µm. (D)

652 Quantification of tracer-filled parenchymal cells in the midbrain between 3 and 6 dpf reveals a

653 significant decrease in tracer uptake at 5 dpf. There was no difference in the number of

654 parenchymal cells that picked up the different tracers at any time point. There was no significant

655 change from 3 to 4 dpf or from 5 to 6 dpf, suggesting that the barrier seals around 5 dpf. N = 10-

656 11 fish, each represented as a single dot on the plot. The mean and the standard error are drawn

657 in black for each tracer and stage. **** $p < 0.0001$, ns is not significant.
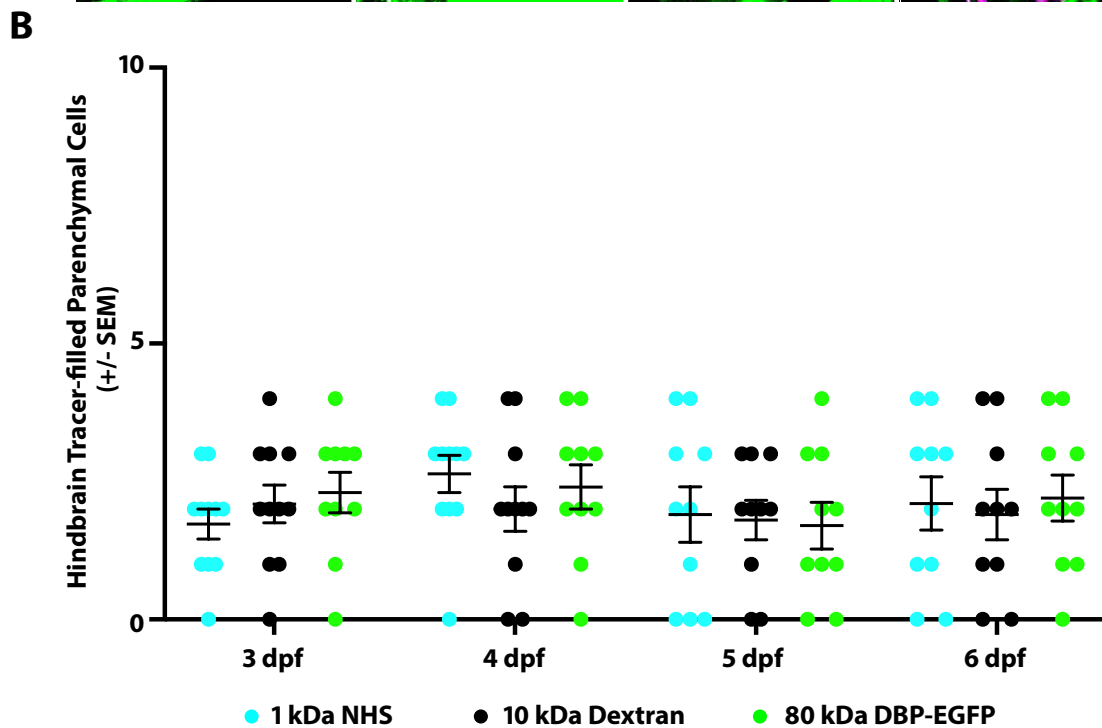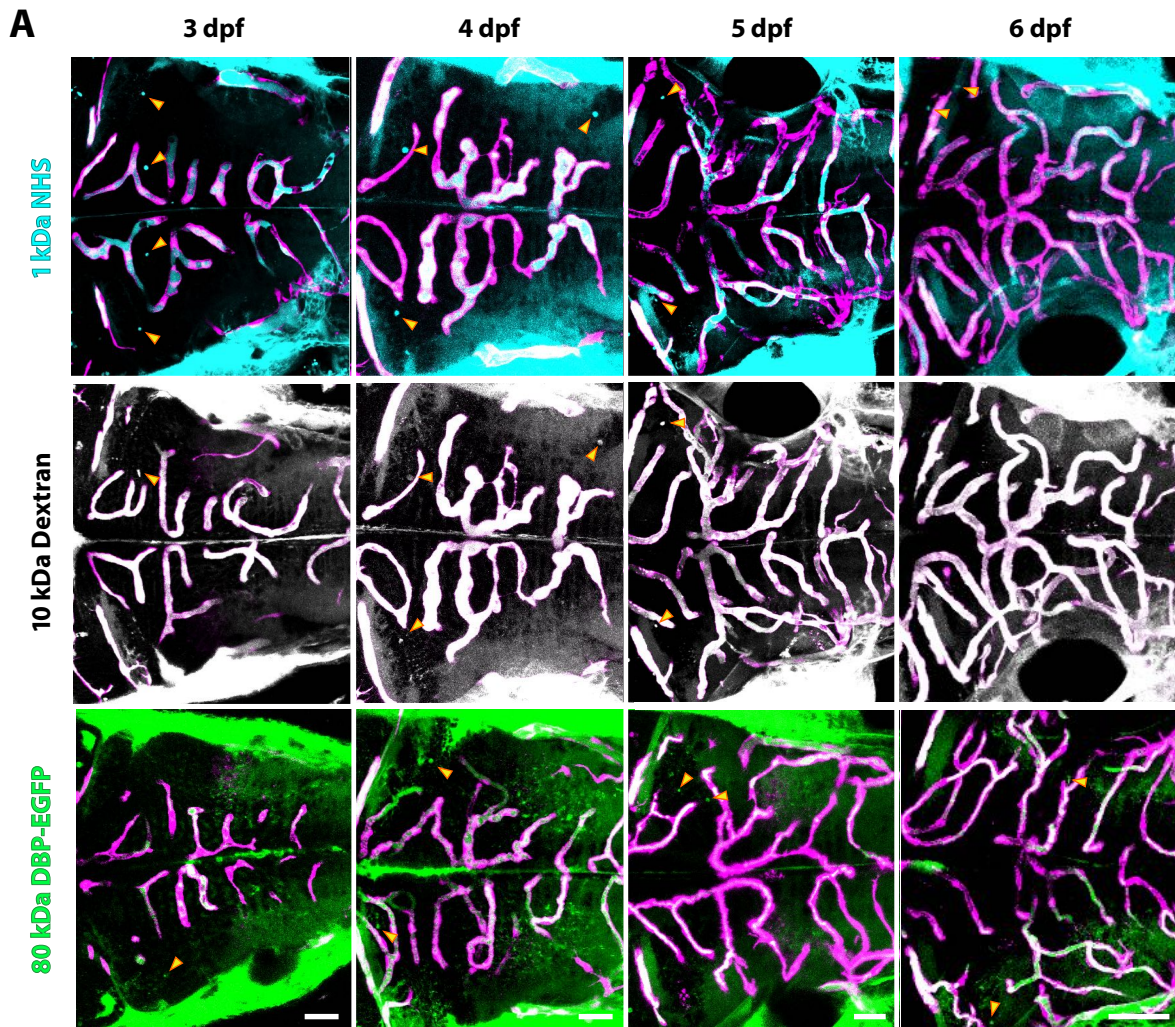
659 **Figure 1 – Supplement 1. The hindbrain has a functional BBB at 3 dpf.** (A) Representative

660 dorsal view maximum intensity projections of larval zebrafish hindbrains at different

661 developmental stages reveals low permeability at 3 dpf that stays constant until 6 dpf. This low

662 permeability was observed with two injected tracers of different sizes, a 1 kDa NHS (turquoise)

663 and a 10 kDa Dextran (white), as well with an 80 kDa transgenic serum protein DBP-EGFP

664 (green). Yellow arrowheads demarcate the few tracer-filled parenchymal cells outside of the

665 vasculature (magenta). Scale bars represent 50 μm. (B) Quantification of tracer-filled

666 parenchymal cells in the hindbrain between 3 and 6 dpf reveals low tracer uptake beginning at 3

667 dpf. There was no difference in the number of parenchymal cells that picked up the different

668 tracers at any time point. N = 10-11 fish, each represented as a single dot on the plot. The mean

669 and the standard error are drawn in black for each tracer and stage.

670

28
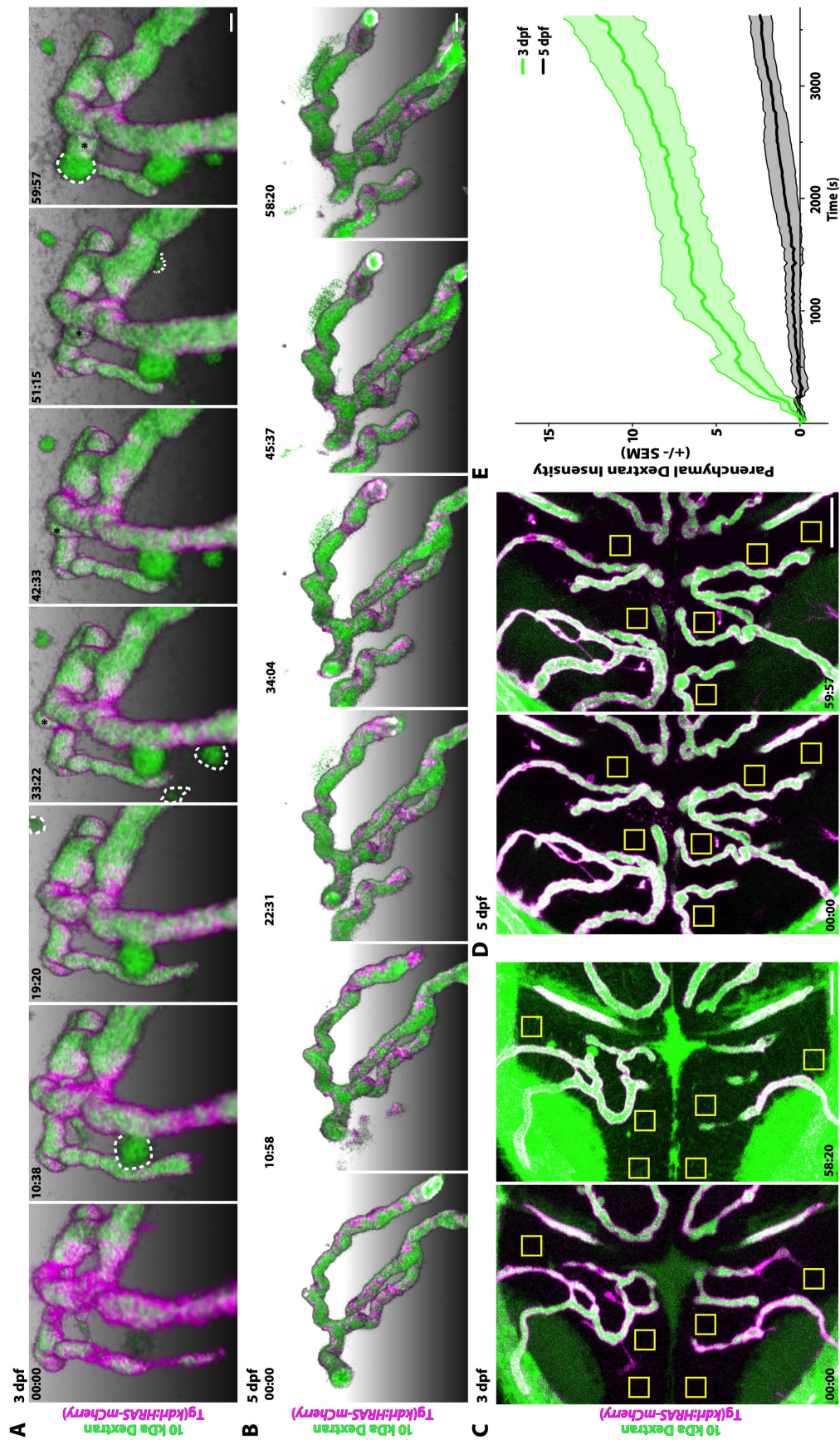
671 **Figure 2. Dynamic tracer leakage in the developing BBB via live imaging.** (A) Time course

672 stills from Video 1 of tracer leakage at 3 dpf reveal an increase in parenchymal cells absorbing

673 the Dextran tracer (outlined by dashed white lines) as well as a general increase in overall Dextran

674 (green) intensity outside of the vasculature (magenta). An angiogenic tip cell becomes apparent

675 at 33:23 and is demarcated by an asterisk (*). This tip cell produces two separate bursts of

676 leakage observed in Video 2. (B) Time course stills of Dextran tracer dynamics at 5 dpf reveals a

677 mature BBB, with reduced overall Dextran extravasation into the brain parenchyma. The scale

678 bars represent 10 μm. (C and D) Dorsal maximum intensity projection of the midbrain at 3 dpf (C)

679 and 5 dpf (D) at the first and last time point examined. While there is a large increase in overall

680 parenchymal Dextran intensity over time at 3 dpf, the 5 dpf midbrain parenchyma appears

681 relatively unaltered after an hour of Dextran circulation. Boxed regions are representative of the

682 six areas per fish used for analysis in E. The scale bars represent 50 μm. (E) Quantification of

683 Dextran intensity in the brain parenchyma over time at 3 dpf (green) and 5 dpf (black) shows a

684 significant difference in tracer leakage dynamics (p<0.0001, Mann Whitney U test), with both more

685 total Dextran accumulation and a faster rate of Dextran accumulation in the brain parenchyma at

686 3 dpf. N=6 fish with 6 regions analyzed per fish.

687
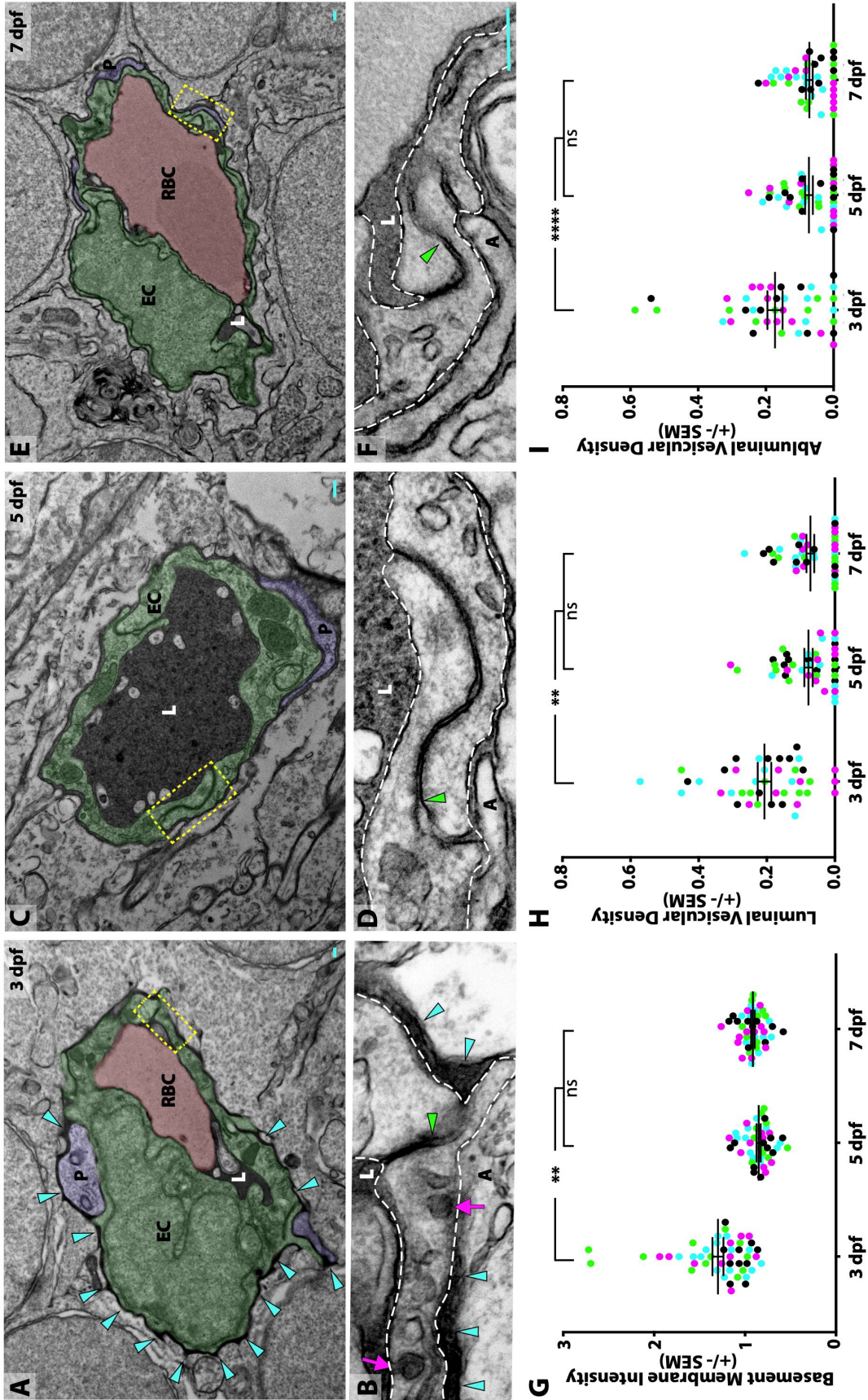
688 **Figure 3. Suppression of transcytosis determines the timing of functional BBB formation.**

689 (A, C, E) TEM images of individual blood vessel cross-sections after injection of electron-dense

690 gold nanoparticles at 3 dpf (A), 5 dpf (C), and 7 dpf (E). Endothelial cells (EC) are pseudo-colored

691 green, pericytes (P) are pseudo-colored purple and red blood cells (RBC) are pseudo-colored red

692 when present in the lumen (L). Turquoise arrowheads highlight the gold-filled basement

693 membrane at 3 dpf (A). (B, D, F) High magnification images (25000x) of the areas boxed in A, C,

694 and E, respectively, with the endothelial cells outlined with white dashed lines. The images are

695 oriented with the lumen (L) on top and the ablumen (A) on the bottom. Tight junctions are

696 functional as early as 3 dpf (B), as seen by their ability to halt the gold nanoparticles at the so-

697 called "kissing point" (green arrowhead), and remain functional throughout development (D and

698 F). Even though the tight junctions are functional at 3 dpf, the endothelial basement membrane is

699 filled with electron-dense gold nanoparticles (B, turquoise arrowheads). This appears to be due

700 to an elevated level of luminal and abluminal gold-filled vesicles (magenta arrows). The scale bars

701 represent 200 nm. (G) Quantification of the endothelial basement membrane gold intensity

702 normalized to luminal gold intensity. (H and I) Quantification of the vesicular densities both on

703 the luminal (H) and abluminal (I) membrane of endothelial cells reveals a suppression of vesicular

704 densities beginning at 5 dpf that remains constant at 7 dpf. N=4 fish, each marked with a different

705 color, with at least 10 blood vessels quantified for each fish. **** p<0.0001, ** p<0.01, ns is not

706 significant.

707
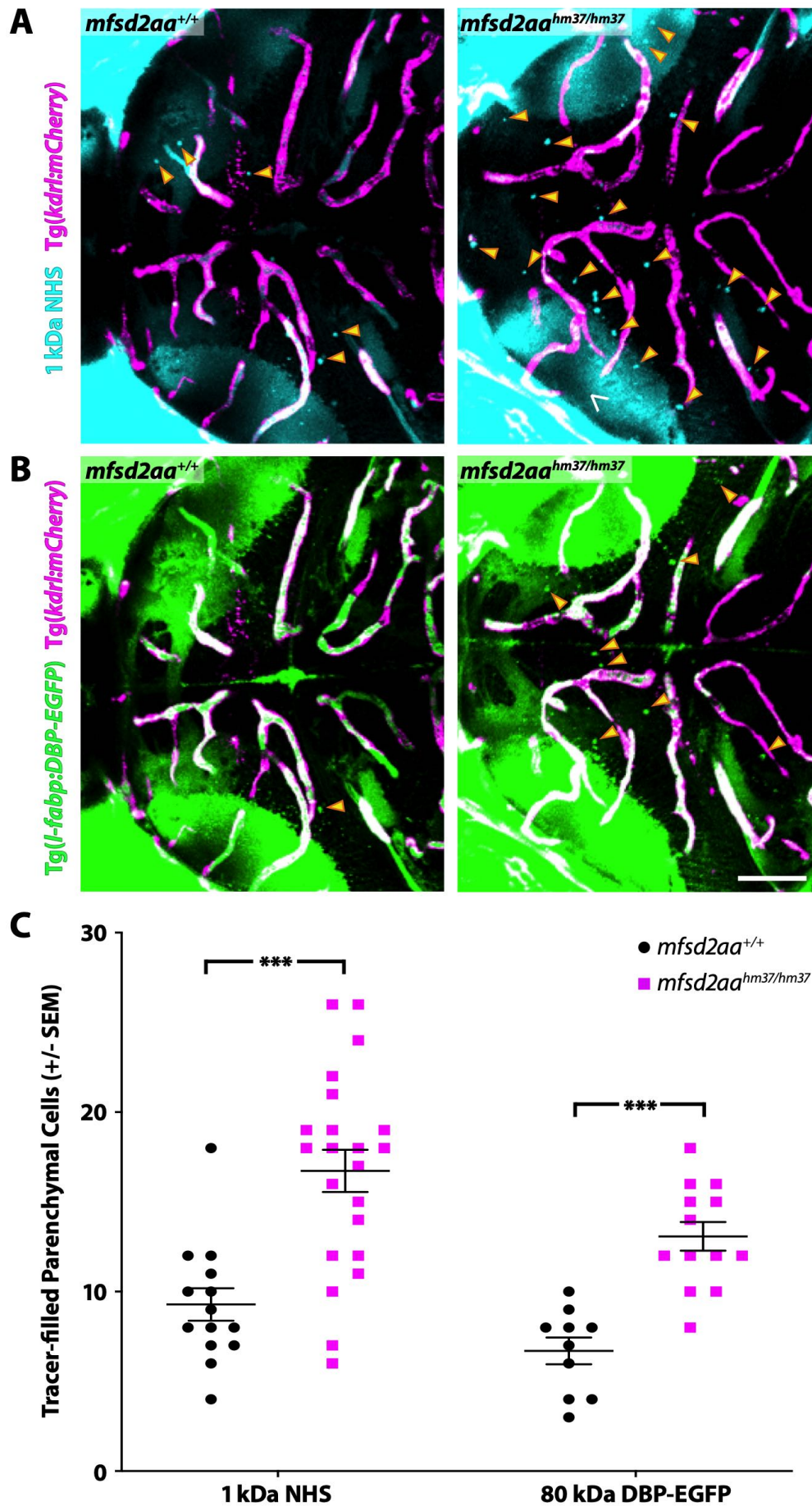
708 **Figure 4. *Mfsd2aa* mutants exhibit increased BBB permeability.** (A) Representative maximum

709 intensity projection images of the midbrain of wildtype and *mfsd2aa* mutants injected with a

710 fluorescent 1 kDa NHS tracer (turquoise) at 5 dpf. *Mfsd2aa* mutants have an increased number

711 of NHS-filled parenchymal cells (yellow arrowheads) that lie outside of the vasculature (magenta;

712 Tg(*kdrl:mCherry*)). (B) Representative maximum intensity projection images of the midbrain of

713 wildtype and *mfsd2aa* mutants expressing the fluorescently labelled 80 kDa transgenic serum

714 protein DBP-EGFP (green) at 5 dpf. *Mfsd2aa* mutants have an increased number of DBP-EGFP-

715 filled parenchymal cells (yellow arrowheads) compared to wildtype siblings. The scale bar

716 represents 50 μm. (C) Quantification of tracer-filled (NHS and DBP-EGFP) parenchymal cells in

717 the midbrain of wildtype (black) and *mfsd2aa* mutants (magenta). *Mfsd2aa* mutants have a

718 significantly increased number of tracer-filled parenchymal cells, both for the injected NHS (A)

719 and the endogenous transgene DBP-EGFP (B). Each individual fish measured is displayed as a

720 single point. The mean and the standard error are drawn as black lines. *** $p < 0.001$, ** $p < 0.01$.

721
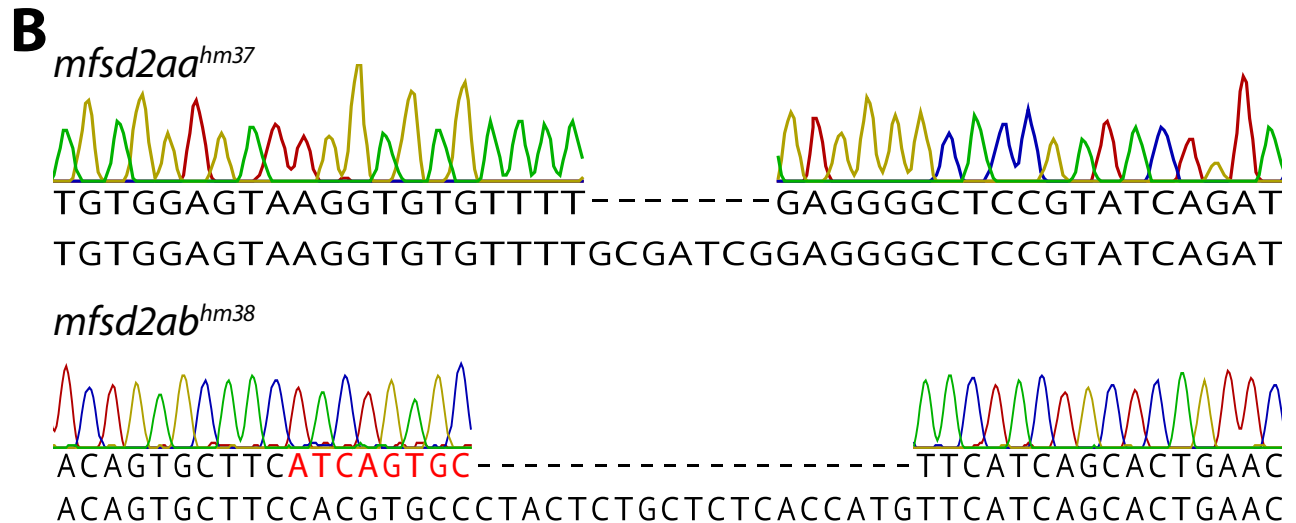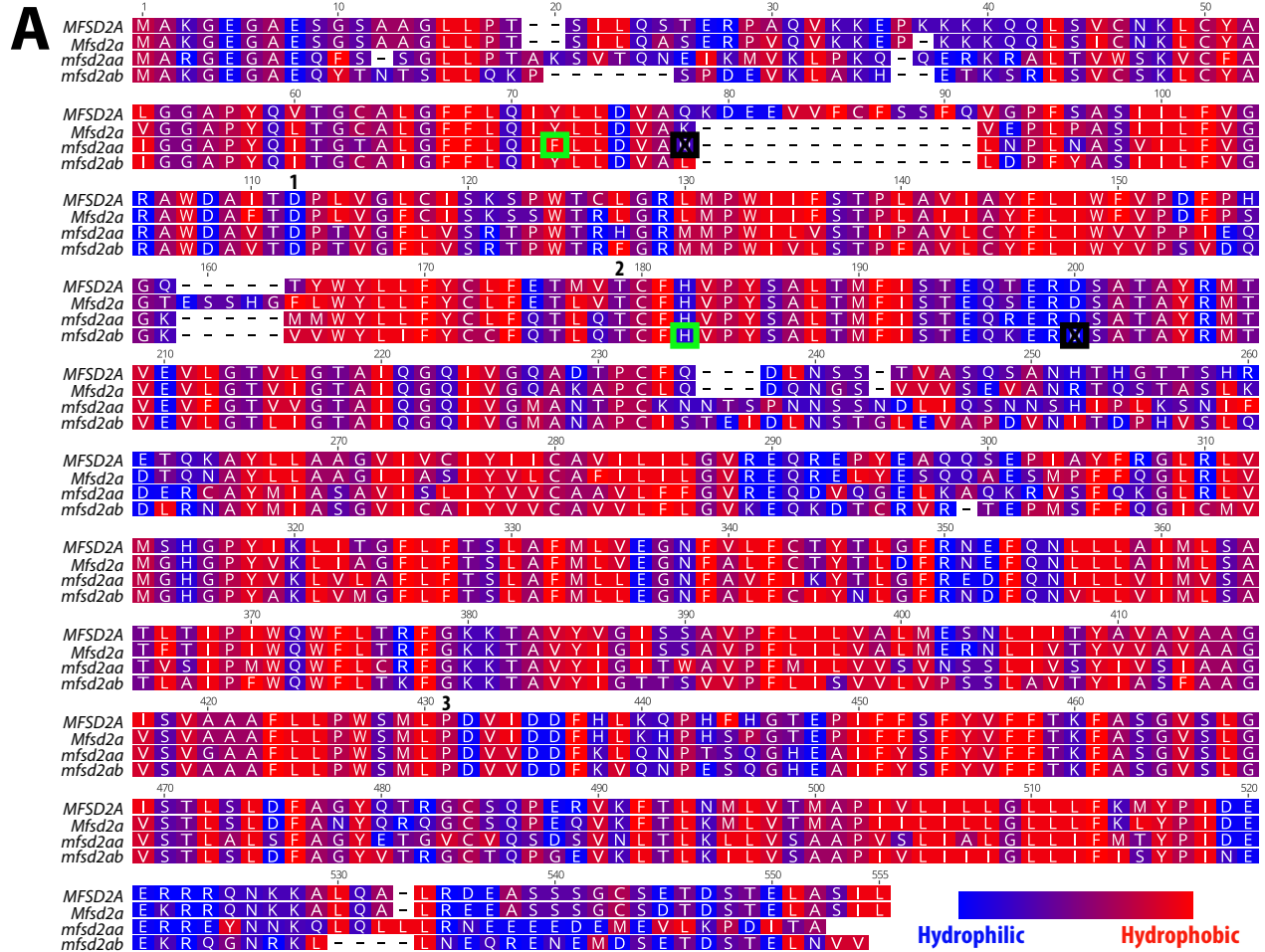
722   **Figure 4 - Supplement 1. Zebrafish have 2 *Mfsd2a* paralogues, *mfsd2aa* and *mfsd2ab*.** (A)

723   Protein alignment of human MFSD2A, mouse Mfsd2a, zebrafish mfsd2aa, and zebrafish mfsd2ab

724   illustrated with a hydrophobicity scale. Red amino acids are hydrophobic and blue amino acids

725   are hydrophilic. Both zebrafish paralogues are highly similar to the human and mouse proteins.

726   Green boxes highlight the genetic lesions in (B) and the black boxes mark the predicted premature

727   stop codons caused by these mutations in *mfsd2aa^hm37/hm37* and *mfsd2ab^hm38/hm38* mutants.

728   Numbers mark amino acid residues with mutations that have been shown to impact Mfsd2a

729   function:1. Andreone et al., 2017, 2. Guemez-Gamboa et al., 2015, 3. Harel et al., 2018. (B)

730   Sanger sequencing of the *mfsd2aa^hm37* and *mfsd2ab^hm38* mutations. *Mfsd2aa^hm37/37* mutants have

731   a 7 base pair deletion in exon 2 that is predicted to lead to a premature stop codon at amino acid

732   82 (A; black box). *Mfsd2ab^hm38/hm38* mutants have an 8 base pair insertion (red letters) and a 19

733   base pair deletion in exon 5 that is predicted to lead to a premature stop codon at amino acid 175

734   (A; black box).

735
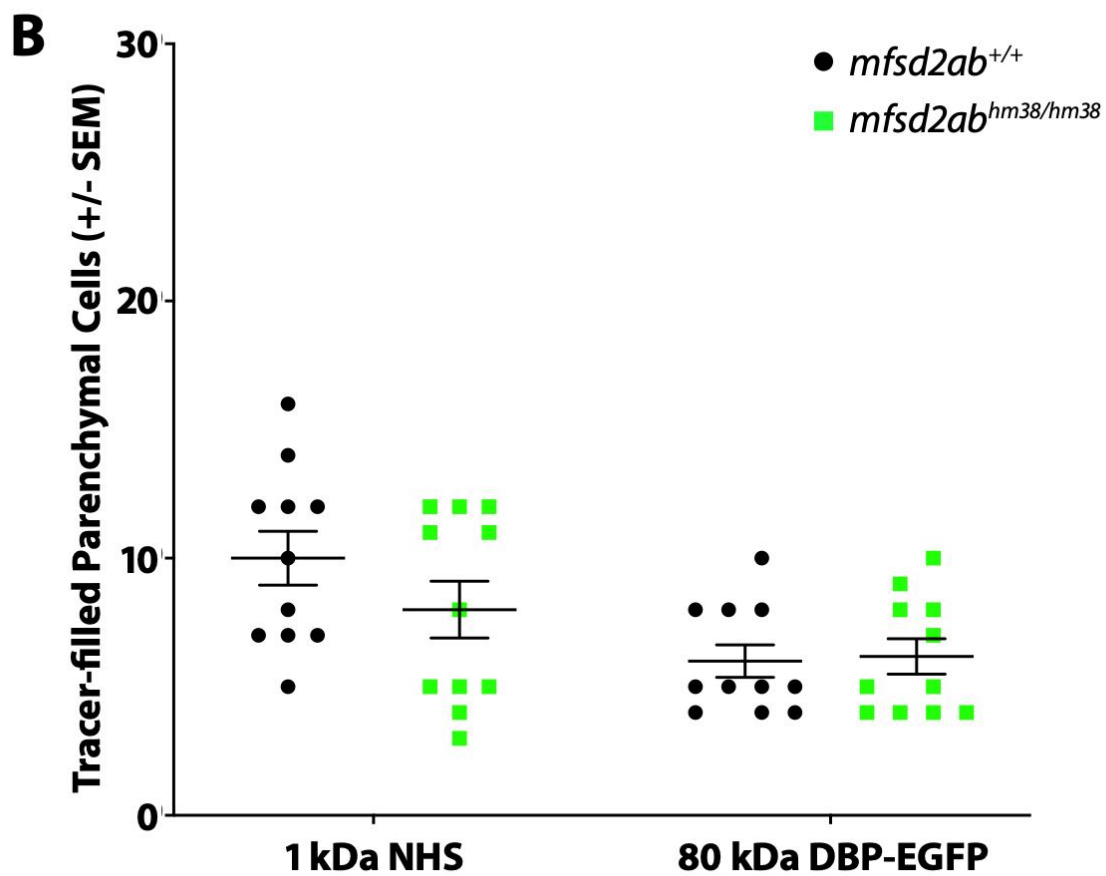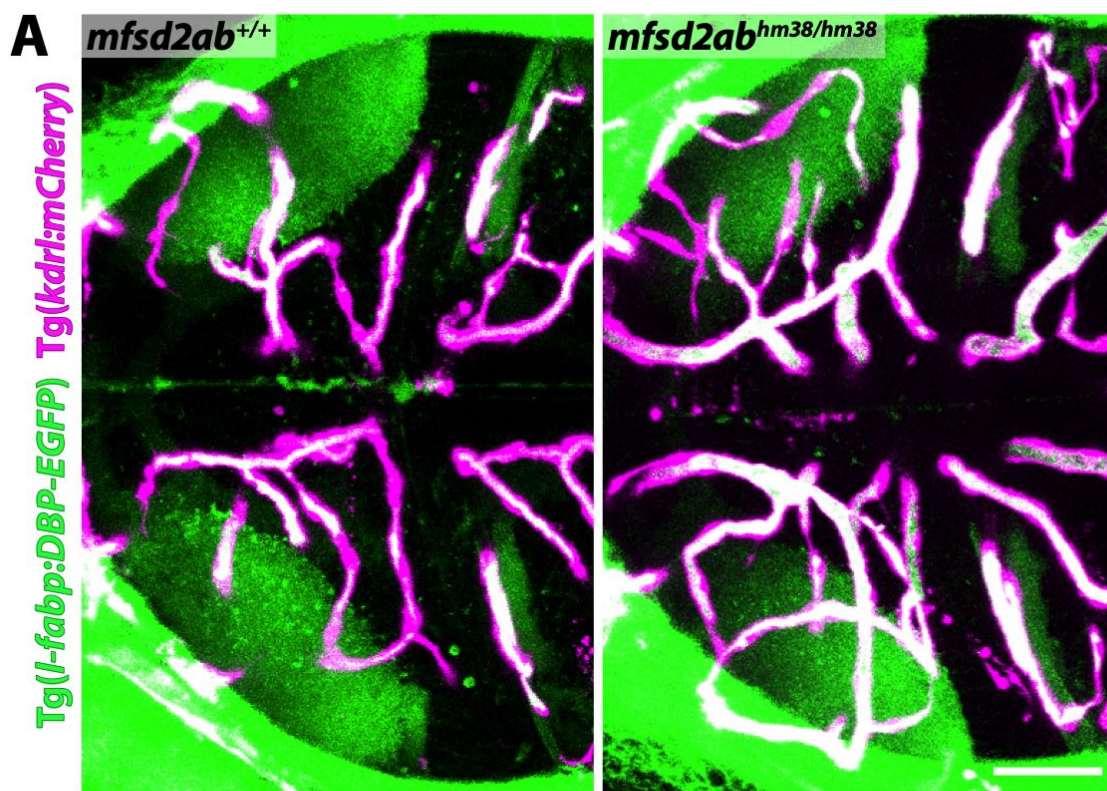
736 **Figure 4 - Supplement 2. *Mfsd2ab* mutants do not have altered BBB permeability.** (A)

737 Representative maximum intensity projection images of the midbrain of wildtype and *mfsd2ab*

738 mutants expressing the fluorescently labelled 80 kDa transgenic serum protein DBP-EGFP

739 (green) at 5 dpf. *Mfsd2ab* mutants have a similarly low number of DBP-EGFP-filled parenchymal

740 cells compared to wildtype siblings. The scale bar represents 50 μm. (B) Quantification of tracer-

741 filled (NHS and DBP-EGFP) parenchymal cells in the midbrain of wildtype (black) and *mfsd2ab*

742 mutants (green). *Mfsd2ab* mutants display no significant barrier permeability defects, both for the

743 injected NHS and the endogenous transgene DBP-EGFP (A). Each individual fish measured is

744 displayed as a single point. The mean and the standard error are drawn in black.

37

745

38
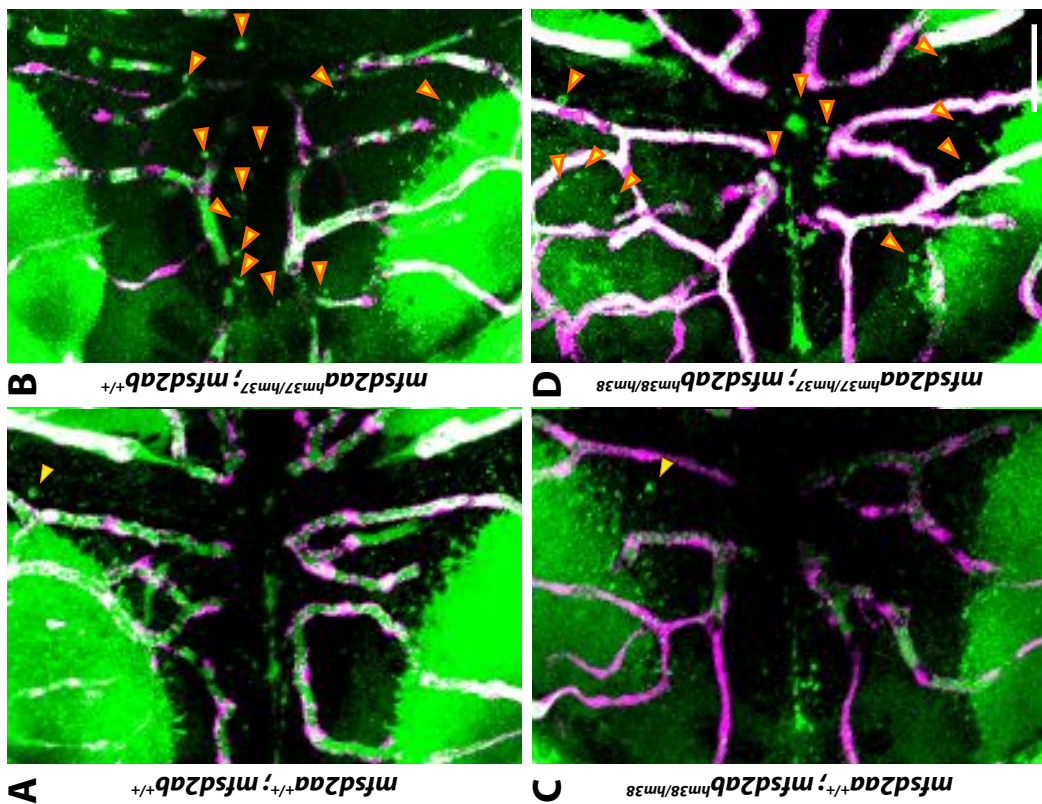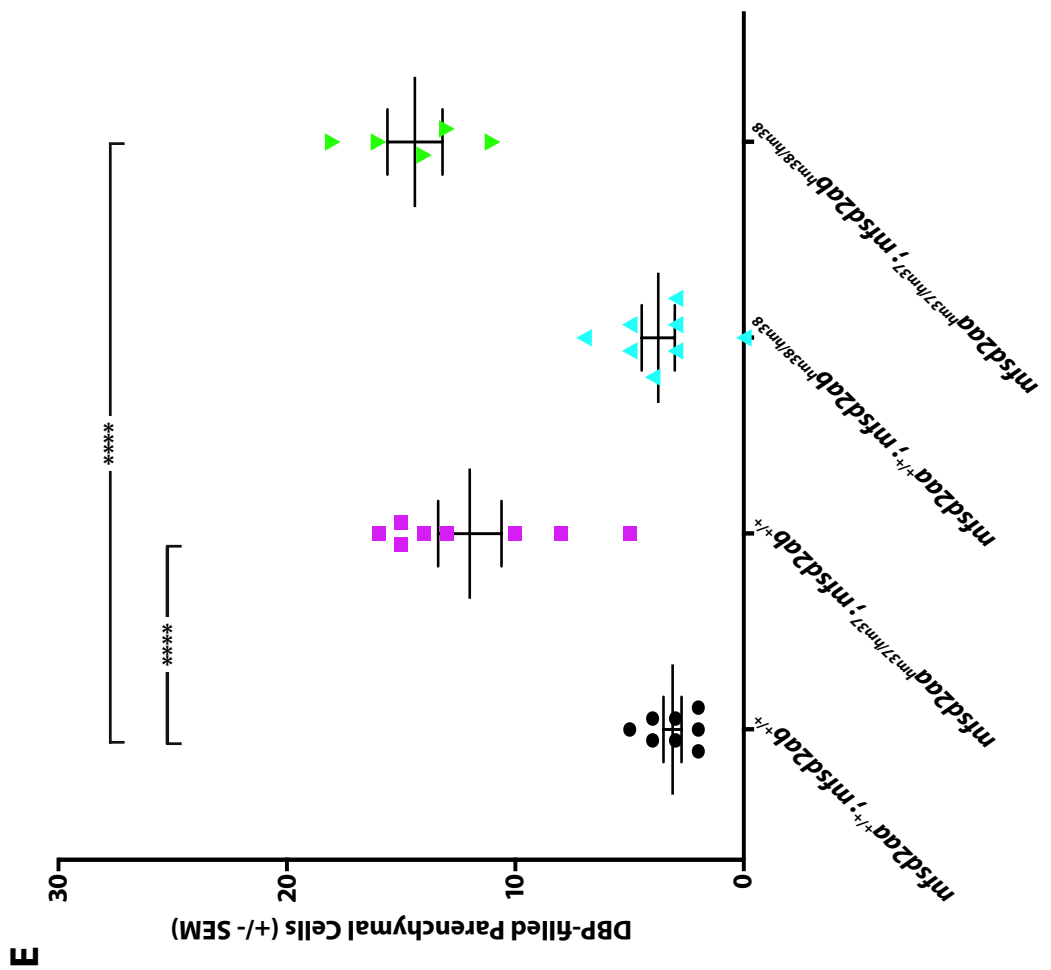
746 **Figure 4 - Supplement 2. *Mfsd2aa$^{hm37/hm37}$; mfsd2ab$^{hm38/hm38}$* double mutants display similar**

747 **increased BBB permeability to *mfsd2aa$^{hm37/hm37}$* fish.** (A-D) Representative maximum intensity

748 projection images of the midbrain of wildtype (A; *mfsd2aa$^{+/+}$; mfsd2ab$^{+/+}$*), *mfsd2aa$^{hm37/hm37}$* single

749 mutants (B), *mfsd2ab$^{hm38/hm38}$* single mutants (C), and *mfsd2aa$^{hm37/hm37}$; mfsd2ab$^{hm38/hm38}$* double

750 mutants (D) expressing the fluorescently labelled 80 kDa transgenic serum protein DBP-EGFP

751 (green) at 5 dpf. *Mfsd2aa$^{hm37/hm37}$; mfsd2ab$^{hm38/hm38}$* double mutants display a similar level of

752 increased tracer-filled parenchymal cells (yellow arrowheads) to the *mfsd2aa$^{hm37/hm37}$* single

753 mutants. The scale bar represents 50 µm. (E) Quantification of DBP-EGFP-filled parenchymal

754 cells in the midbrain of wildtype (black), *mfsd2aa$^{hm37/hm37}$* mutants (magenta), *mfsd2ab$^{hm38/hm38}$*

755 mutants (turquoise), and *mfsd2aa$^{hm37/hm37}$; mfsd2ab$^{hm38/hm38}$* double mutants (green). Each

756 individual fish measured is displayed as a single point. The mean and the standard error are

757 drawn in black. **** $p < 0.0001$.

758

759

760

40
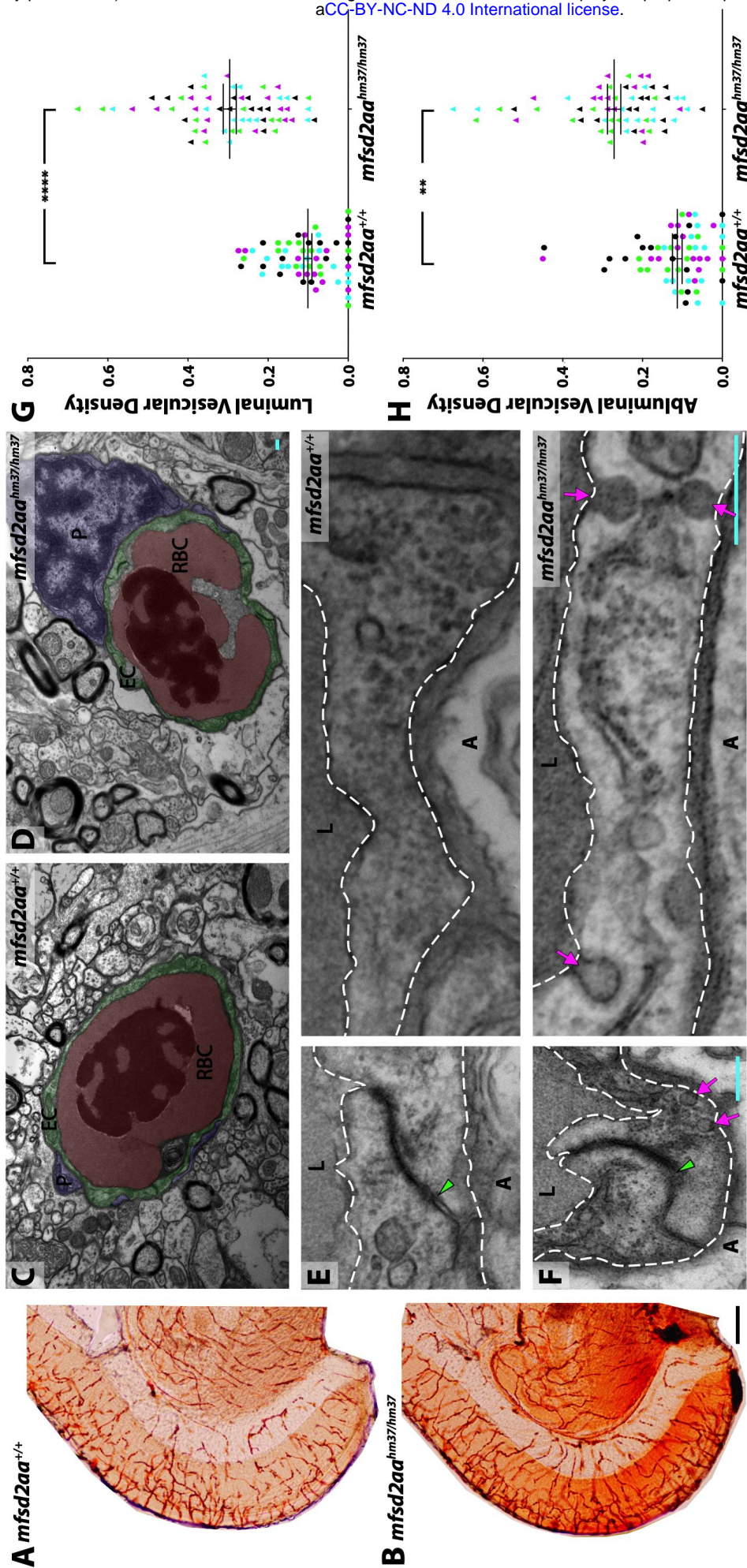
761 **Figure 5. M*fsd2aa* mutants exhibit increased transcytosis.** (A and B) Coronal sections of adult

762 midbrain after 30 minutes of HRP (brown) circulation in wildtype (A) and *mfsd2aa* mutant fish (B).

763 Wildtype adults confine the HRP within the blood vessels, but *mfsd2aa* mutants leak HRP into

764 the brain parenchyma. The scale bar represents 200 μm. (C and D) TEM images of individual

765 blood vessel cross-sections of adult wildtype (C) and *mfsd2aa* mutant fish (D). Endothelial cells

766 (EC) are pseudo-colored green, pericytes (P) are pseudo-colored purple and red blood cells

767 (RBC) are pseudo-colored red. (E and F) High magnification images of endothelial cells outlined

768 with white dashed lines of wildtype (E) and *mfsd2aa* mutants (F). The images are oriented with

769 the lumen (L) on top and the ablumen (A) on the bottom. *Mfsd2aa* mutants appear to have normal

770 tight junctions (green arrowhead) but elevated levels of luminal and abluminal vesicles (magenta

771 arrows). The scale bars represent 200 nm. (G and H) Quantification of the vesicular densities

772 both on the luminal (G) and abluminal (H) side of the endothelial cells reveals that *mfsd2aa*

773 mutants have increased vesicular densities. N=4 fish, each marked with a different color, with 15

774 blood vessels quantified for each fish. **** $p < 0.0001$, ** $p < 0.01$.
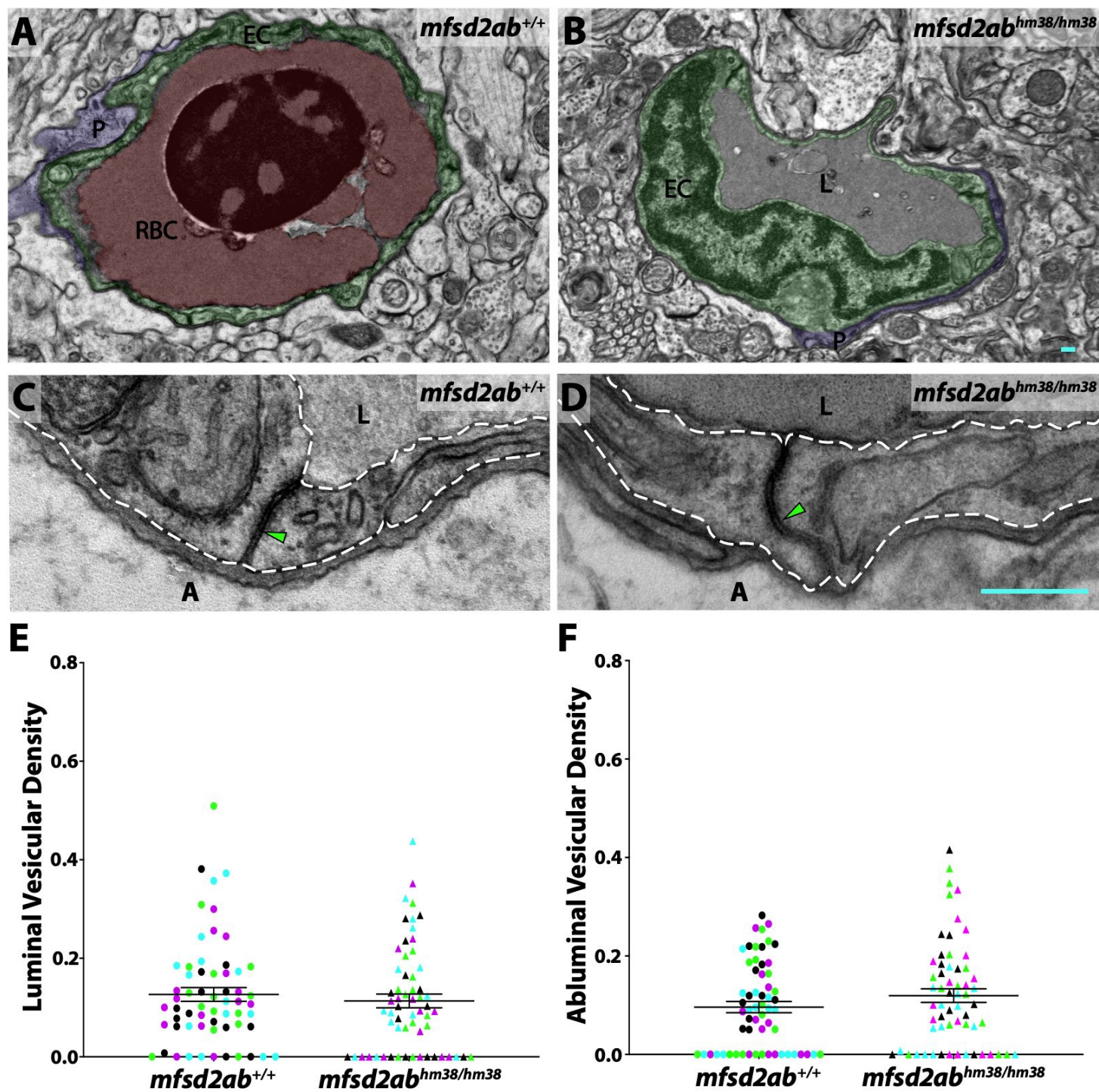
775

776

777 **Figure 5 - Supplement 1. M*fsd2ab* mutants exhibit normal vascular maturation.** (A and B)

778 TEM images of individual blood vessel cross-sections of adult wildtype (A) and *mfsd2ab* mutants

779 (B). Endothelial cells (EC) are pseudo-colored green, pericytes (P) are pseudo-colored purple

780 and red blood cells (RBC) are pseudo-colored red when present in the lumen (L). (C and D) High

781 magnification images of endothelial cells outlined with white dashed lines of wildtype (C) and

782 *mfsd2ab* mutants (D). The images are oriented with the lumen (L) on top and the ablumen (A) on

783 the bottom. *Mfsd2ab* mutants appear to have normal tight junctions (green arrowhead) and levels

784 of luminal and abluminal vesicles. The scale bars represent 200 nm. (E and F) Quantification of

785 the vesicular densities both on the luminal (E) and abluminal (F) side of the endothelial cells

786 reveals that *mfsd2ab* mutants have similar vesicular densities to wildtype siblings. N=4 fish, each

787 marked with a different color, with 15 blood vessels quantified for each fish.